VIROLOGY

Airborne fine particles drive H1N1 viruses deep into the lower respiratory tract and distant organs

Zheng Dong[1,2], Juan Ma[1,2], Jiahuang Qiu[1,2], Quanzhong Ren[1,3], Qing'e Shan[1,4], Xuefeng Duan[5], Guangle Li[6], Yi Y. Zuo[6], Yu Qi[1,2], Yajun Liu[7], Guoliang Liu[8,9], Iseult Lynch[10], Min Fang[5]*, Sijin Liu[1,2,4]*

Mounting data suggest that environmental pollution due to airborne fine particles (AFPs) increases the occurrence and severity of respiratory virus infection in humans. However, it is unclear whether and how interactions with AFPs alter viral infection and distribution. We report synergetic effects between various AFPs and the H1N1 virus, regulated by physicochemical properties of the AFPs. Unlike infection caused by virus alone, AFPs facilitated the internalization of virus through a receptor-independent pathway. Moreover, AFPs promoted the budding and dispersal of progeny virions, likely mediated by lipid rafts in the host plasma membrane. Infected animal models demonstrated that AFPs favored penetration of the H1N1 virus into the distal lung, and its translocation into extrapulmonary organs including the liver, spleen, and kidney, thus causing severe local and systemic disorders. Our findings revealed a key role of AFPs in driving viral infection throughout the respiratory tract and beyond. These insights entail stronger air quality management and air pollution reduction policies.

INTRODUCTION

Exposure to airborne fine particles (AFPs) has been linked to increased morbidity and mortality of respiratory viruses (1), including the severe acute respiratory syndrome coronavirus 2 (SARS-CoV-2) (2, 3). AFPs have also been shown to promote the spread of *Streptococcus pneumoniae* from the nasopharynx to the lung in mice and enhance the replication of human polyomavirus (4, 5). Furthermore, a few studies to date have identified diverse viral nucleic acids in ambient AFPs, suggesting that AFPs are likely important vehicles for pathogen transmission (6, 7). These observations are of substantial importance, because smaller-sized or ultrafine AFPs are recognized to cross the air-blood barrier and accumulate in distant organs, such as the knee joint and even brain in humans and animals (8–11). Infection of extrapulmonary organs by highly pathogenic influenza A viruses (IAVs), e.g., the H5N1 and H7N9 strains (12, 13), have also been detected, despite the viral exposure and transport pathway warranting detailed investigation.

In the presence of AFPs, viruses could incur more severe infection by disrupting epithelial barriers or altering immune homeostasis (14–16). More recently, AFPs were reported to elevate the expression of the SARS-CoV-2 receptor, angiotensin-converting enzyme 2, and enhance virus entry via the receptor-dependent route (17, 18). While it is known that physicochemical properties such as size of inhaled AFPs can decide where they accumulate along the airway (19), how AFPs interact with viruses and whether the interactions influence viral infectivity, replication, release, and dispersal are still unclear (20, 21). Understanding the impact of AFPs on virus infection and biodistribution could have considerable implications for air pollution and disease management.

In this regard, we aimed to shed light on the synergistic outcomes between H1N1 viruses and different types of AFPs in vitro and in vivo. To gain a general understanding of the AFP properties responsible for respiratory virus infection, we deliberately selected four representative AFPs with diverse sources and compositions in the current study. First, particulate matter with a diameter smaller than 2.5 µm (PM2.5) was sampled from the atmospheric environment. Second, dust particles with silicon dioxide (SiO_2) as the main constituent were selected, standing for AFPs originating from sandstorms, mineral dust, and so on (22, 23). Third, biochar particles were prepared through biomass burning, representing AFPs released from biomass fuel consumption, wildfires, and so forth (24, 25). Last, carbon black particles were produced from the combustion of natural gas, representing AFPs emitted from fossil fuel combustion in traffic and industrial activities (26, 27). Our selected AFPs exhibited a broad range of physicochemical properties, including wide variation in surface area and pore volume, differential morphology, and varied surface hydrophobicity. Here, our data unveiled that AFP-virus interactions largely relied on the AFP physicochemical properties, which essentially altered the infection and distribution of loaded viruses. To a differential extent, all AFPs were found to reinforce virus uptake, replication, and release, and to drive viral transport to extrapulmonary organs including the liver, spleen, and kidney. As a consequence, AFPs were uncovered to worsen the severity of viral infection in mice. Together, our findings highlight the remarkable contribution of AFPs to virus transmission and infection, and provide an avenue to further scrutinize

[1]State Key Laboratory of Environmental Chemistry and Ecotoxicology, Research Center for Eco-Environmental Sciences, Chinese Academy of Sciences, Beijing 100085, China. [2]University of Chinese Academy of Sciences, Beijing 100049, China. [3]Beijing Key Laboratory of Environmental Toxicology, Capital Medical University, Beijing 100069, China. [4]Medical Science and Technology Innovation Center, Shandong First Medical University & Shandong Academy of Medical Sciences, Jinan, Shandong 250117, China. [5]CAS Key Laboratory of Pathogenic Microbiology & Immunology, Institute of Microbiology, Chinese Academy of Sciences, Beijing 100101, China. [6]Department of Mechanical Engineering, University of Hawaii at Mānoa, Honolulu, HI 96822, USA. [7]Beijing Jishuitan Hospital, Peking University Health Science Center, Beijing 100035, China. [8]Department of Pulmonary and Critical Care Medicine, Centre for Respiratory Diseases, China-Japan Friendship Hospital, Beijing 100029, China. [9]National Center for Respiratory Medicine, Beijing 100029, China. [10]School of Geography, Earth and Environmental Sciences, University of Birmingham, Birmingham B15 2TT, UK.
*Corresponding author. Email: sjliu@rcees.ac.cn (S.L.); fangm@im.ac.cn (M.F.)

the behavior and fate of viruses upon interaction with and loading onto AFPs.

RESULTS

Active association between AFPs and H1N1 viruses

First, we studied the interaction of human influenza virus A/Puerto Rico/8/34 (H1N1 PR8) with naturally sampled PM2.5, silica-based particles (i.e., dust), and carbon-based particles (i.e., biochar and carbon black) (as illustrated in Fig. 1A). Transmission electron microscopy (TEM) and scanning EM (SEM) images showed the size ranges of PM2.5 (300 to 2000 nm), dust (500 to 6000 nm), biochar (200 to 3200 nm), and carbon black (20 to 90 nm) (fig. S1, A and B). As characterized by the Brunauer-Emmett-Teller analysis (fig. S1C), the surface area and micropore volume of AFPs ranked in the order: carbon black > PM2.5> biochar > dust. X-ray photoelectron spectroscopy analysis of surface chemistry demonstrated that PM2.5, dust, and biochar bore relatively abundant oxygen-containing functional groups (C—O and O═C—O), while carbon black contained the least of all studied AFPs (fig. S1, D and E). In addition, the hydrophilicity and hydrophobicity of these particles were determined through the dye partitioning method with a hydrophilic dye (Nile Blue, NB) and a hydrophobic dye (Rose Bengal, RB), respectively. Our data suggested that carbon black was the most hydrophobic
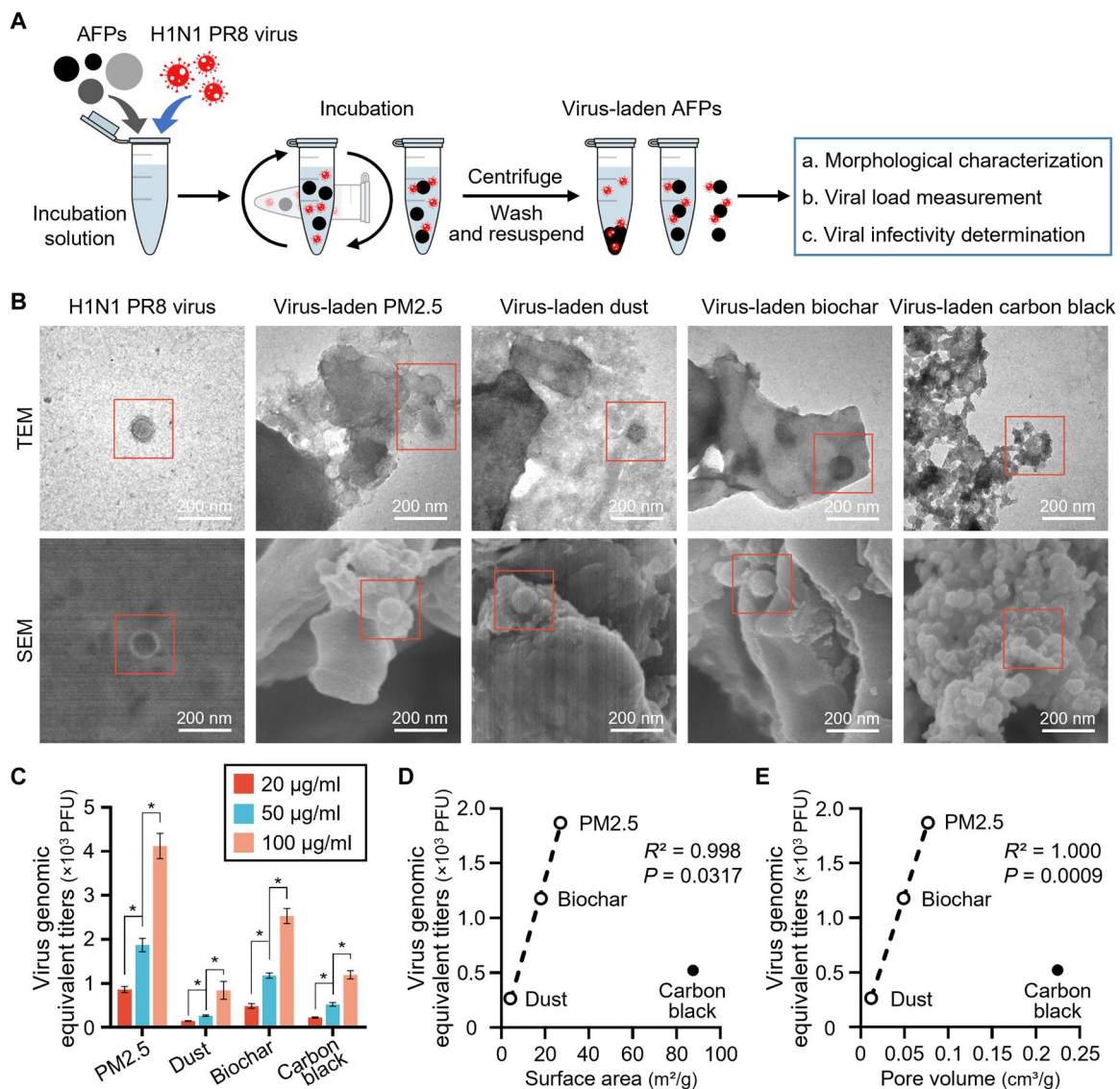

Fig. 1. AFPs interact with and load H1N1 viruses. (**A**) Schematic diagram showing the preparation of virus-laden airborne fine particles (AFPs). Here, AFPs [50 μg/ml of each; particulate matter with a diameter smaller than 2.5 μm (PM2.5), dust, biochar, and carbon black] were incubated with 1.0×10^4 plaque-forming unit (PFU) H1N1 PR8 viruses for 1 hour and washed three times with phosphate-buffered saline (PBS) before examination of morphology, viral load, and infectivity. (**B**) Transmission electron microscopy (TEM; top panel) and scanning EM (SEM; bottom panel) images show that H1N1 PR8 viruses (denoted by red squares) are adsorbed into the surface of PM2.5, dust, and biochar but are enveloped by carbon black particles. (**C**) Quantitative real-time polymerase chain reaction (qRT-PCR) analysis of viral loads on AFPs at 20, 50, and 100 μg/ml (n = 3). Viral load for each AFP was obtained by converting cycle threshold (Ct) values using the standard curves (fig. S3). (**D** and **E**) Correlation analysis between (D) surface area and (E) pore volume of AFPs and viral loads on AFPs (50 μg/ml). Pearson correlation (R^2) and statistical significance (P value) are shown. *$P < 0.05$.

of the four AFPs, whereas PM2.5, dust, and biochar appeared to be more hydrophilic (fig. S2, A and B).

As seen in the negative-stained TEM images (Fig. 1B), the H1N1 PR8 virus was spherical and contained condensed ribonucleoprotein inside a well-resolved lipid envelope decorated with microspike projections, as reported (28). Even after extensive washing, intact viruses could still be visualized on all AFPs, indicating robust and sustained interaction between H1N1 PR8 viruses and AFPs. On closer inspection, we observed that virus particles were mainly adsorbed into the micropores of PM2.5, dust, and biochar but were wrapped by or embedded between carbon black particles (Fig. 1B), hinting at a different association mode between carbon black and viruses.

To determine the viral loads on different AFPs, we measured the viral matrix protein 1 (*M1*) gene using quantitative real-time polymerase chain reaction (qRT-PCR), as established (29–31). The viral load for each AFP sample was obtained by converting the cycle threshold (Ct) values (namely, the cycle number at which the PCR product exceeds the set threshold) using the standard curve generated from known virus titers (fig. S3). All AFPs showed concentration-dependent viral loads ($P < 0.05$; Fig. 1C). Of note, PM2.5 adsorbed much more viruses than the other three AFPs with two- to sevenfold ($P < 0.05$; Fig. 1C), and biochar ranked second in viral loading, showing approximately two- to fourfold greater viral loads than carbon black and dust, respectively ($P < 0.05$; Fig. 1C).

Further correlation analyses revealed that viral loading closely correlated to the physicochemical properties of AFPs (Fig. 1, D and E). PM2.5 with higher surface area and larger pore volumes displayed higher viral loading than dust and biochar ($P < 0.05$). Otherwise, consistent with the different patterns of AFP-virus interaction illustrated in Fig. 1B, carbon black was not clustered with the other three AFPs in the correlation analyses (Fig. 1, D and E), implying a discrepant association mode for carbon black that only to a less extent was decided by surface area and pore volume, but likely to a greater extent by other factors including size, morphology, and hydrophobicity. This discrepancy warrants more detailed further investigations. Collectively, these results suggested an active association between AFPs and H1N1 viruses that was regulated by the AFP physicochemical properties, and of them, the area and volume of the contact interface dictated virus loading onto AFPs (including PM2.5, dust, and biochar), except for carbon black with a different particle-virus interaction pattern.

AFP-borne H1N1 viruses remain infectious
To determine whether viruses loaded onto AFPs remain alive and infectious, we examined the viral hemagglutinin (HA) activity upon interaction with AFPs using the classical hemagglutination assay (32). HA is a glycoprotein on the virus surface that initiates infection, and hemagglutination is observed when the viruses cross-link with red blood cells (RBCs). Similar to H1N1 PR8 viruses (virus control), all AFP-virus complexes agglutinated RBCs (Fig. 2A). Approximately 70 to 90% of the viral HA activity stayed after 4 hours of incubation (Fig. 2B), demonstrating that AFPs had only a mild effect on viral HA activity.

We further looked at the infectivity of AFP-borne viruses using the standard plaque assay (6). Madin-Darby canine kidney (MDCK) monolayer cells infected with solo viruses (namely, the free virus control) or AFP-borne viruses formed plaques, indicating that AFP-borne viruses remained infectious (Fig. 2, C and D). The number of virus plaques elevated with increasing concentration of virus-laden AFPs ($P < 0.05$; Fig. 2C). Consistent with the viral loads shown in Fig. 1C, PM2.5-borne viruses gave rise to two- to fivefold more plaques than the other three AFPs at the same concentration ($P < 0.05$; Fig. 2, C and D). Together, these data qualitatively and quantitatively indicated that viruses bound to AFPs remained infectious.

To verify the infectivity of AFP-borne viruses, we used lung epithelial A549 cells, a sialic acid (SA) receptor-positive cell line commonly used for IAV infection analyses (33), to study the viral lifecycle, including internalization, replication, and release under different conditions (Fig. 2E). Consistent with the IAV infection pattern reported previously (34, 35), the solo viruses showed effective entry into target cells after a 1-hour infection (Fig. 2F). For the single cycle (8 hours post infection, hpi) and multicycle (24 and 48 hpi) virus replication kinetics (31), the levels of intracellular viruses (indicative of newly synthesized virions) increased progressively over time ($P < 0.001$; Fig. 2F). Moreover, the titers of extracellular viruses (suggestive of released mature virus progeny) displayed a similar incremental trend corresponding to the intracellular virus titers ($P < 0.05$). Notably, similar results were demonstrated in primary human small airway epithelial cells (hSAECs; fig. S4A).

When cells were incubated with AFP-borne viruses at 37°C for 1 hour, we found that viruses adsorbed onto AFPs (especially PM2.5) had already entered cells ($P < 0.001$; Fig. 2G). The contents of intracellular viruses and extracellular viruses quantified after a single cycle and multiple cycles of infection manifested progressive increases ($P < 0.05$; Fig. 2, H and I). The increase in viral titers revealed that AFP-borne viruses were replicating within A549 cells and releasing mature viral progeny over time. Overall, PM2.5 induced significantly more virus entry, replication, and subsequent release than the other AFPs ($P < 0.05$; Fig. 2, G to I), in agreement with the greater viral loading as described in Fig. 1C. Consistent findings were also confirmed in hSAECs (fig. S4, B to D).

Flow cytometry analysis of A549 cells infected with enhanced green fluorescent protein (EGFP)–tagged viruses or AFP-borne viruses substantiated intracellular accumulation of newly synthesized virions (EGFP-positive cells) in a time-dependent manner ($P < 0.001$; Fig. 2J and fig. S5). Consistent with qRT-PCR data, flow cytometry data also unveiled that PM2.5 induced a greater proportion of EGFP-positive cells than the other three AFPs with two- to threefold ($P < 0.001$; Fig. 2J and fig. S5B). The correlation analysis indicated that the percentage of EGFP-positive viable cells was significantly positively correlated with the contents of newly replicated viruses ($P < 0.001$; Fig. 2K). Together, our results uncovered that AFPs delivered viruses to host cells for effective internalization, replication, and release. PM2.5, which had higher viral loads, consistently elicited greater effects than dust, biochar, and carbon black.

AFPs are implicated in the initial transport of viruses into target cells
To decipher how AFPs participate in the lifecycle of H1N1 viruses, we immunostained the viruses with an anti-HA antibody (red) and observed their interactions with AFPs and target cells using laser scanning confocal microscopy (LSCM). High-magnification LSCM images showed that AFP-borne viruses (red) readily entered cells at sites where AFPs (black) were localized close to the plasma membrane at 1 hpi (yellow arrowheads in Fig. 3A), hinting that AFPs likely acted as a Trojan horse for viral entry

Fig. 2. AFP-borne viruses remain infectious in vitro. (**A**) Viral hemagglutinin (HA) activity assay involves coincubation of viruses and standardized concentration of red blood cells (RBCs; top illustration). Experimental data (bottom panel) showed that RBCs were agglutinated after incubation with solo viruses (virus control) or AFP-virus complexes for 4 hours. (**B**) Relative HA activity of AFP-borne viruses after 4 hours of incubation (*n* = 5). AFP concentration is 50 μg/ml, and virus titer is 1.0×10^6 PFU. (**C**) Numbers of plaques formed in Madin-Darby canine kidney (MDCK) cells treated with virus-laden AFPs (20, 50, and 100 μg/ml; *n* = 3). (**D**) Representative images of viral plaques. MDCK cells were infected with solo viruses (at 200 PFU) or virus-laden AFPs (50 μg/ml) and stained with crystal violet following a 48-hour infection. Yellow arrowheads denote viral plaques. (**E**) Schematic showing internalized (37°C for 1 hour), replicated, and released viruses (8, 24, and 48 hours post infection, hpi) in AFP-borne virus-infected target cells. (**F**) Quantification of internalized, replicated, and released viruses in A549 cells infected with solo viruses (at 200 PFU) through qRT-PCR assay (*n* = 4). (**G** to **I**) Quantification of (G) internalized, (H) replicated, and (I) released viruses in AFP-borne virus-infected A549 cells (*n* = 4). (**J**) Flow cytometry data (left) and corresponding quantitative analysis (right) of A549 cells infected with enhanced green fluorescent protein (EGFP)–tagged viruses bound onto AFPs at 24 hpi (*n* = 4). SSC-H, side scatter height. (**K**) Correlation analysis between replicated viruses and EGFP-positive cell percentage in viable cells at 8, 24, and 48 hpi. Pearson correlation (R^2) and statistical significance (*P* value) are shown. *$P < 0.05$; **$P < 0.001$.
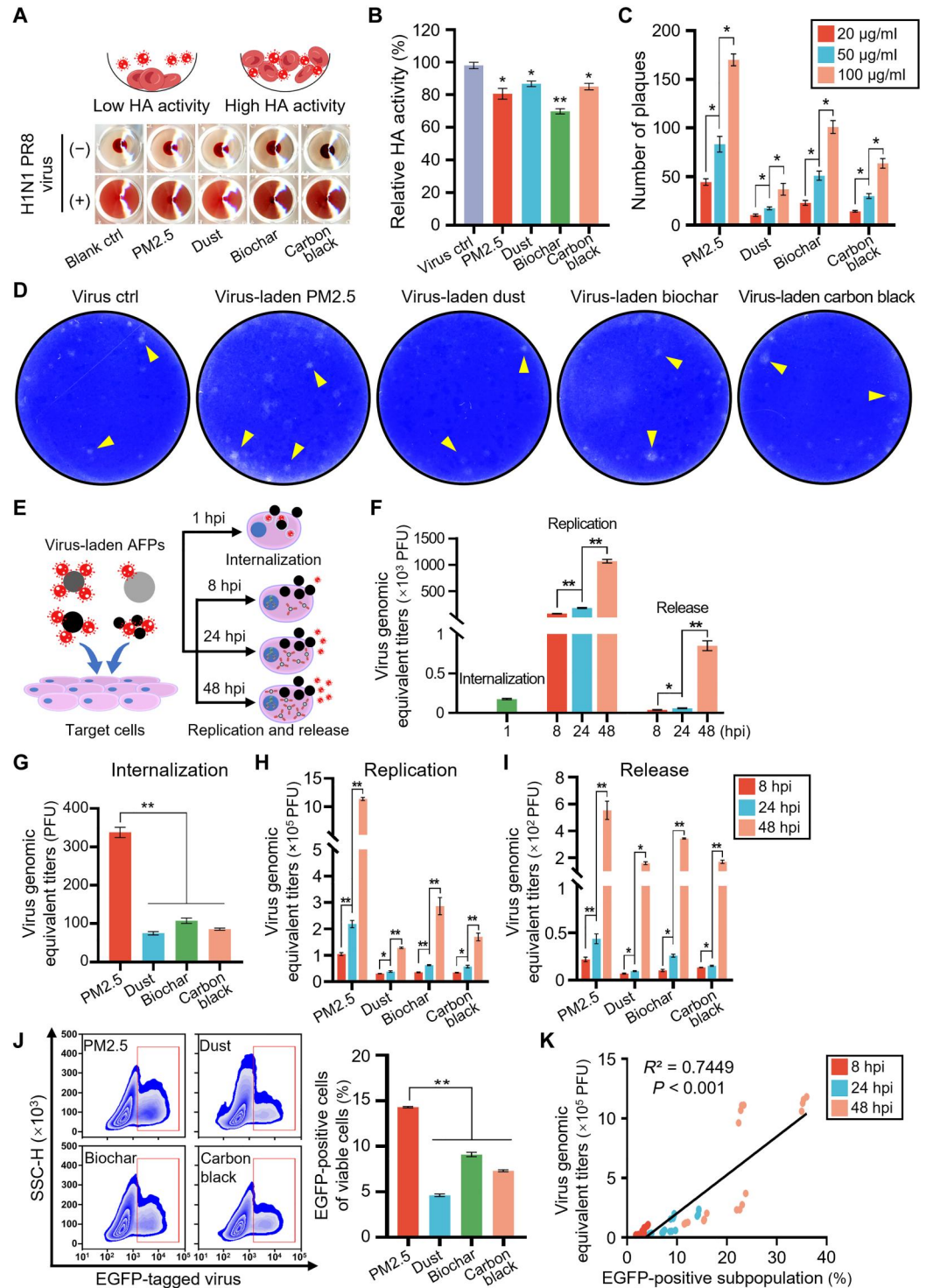
into host cells at the early stages of infection. Likewise, similar results were determined in hSAECs (fig. S6). To interrogate whether AFP-borne virus infection is receptor-mediated, we treated A549 cells with neuraminidase (NA) enzyme to remove the surface SA groups that are indispensable for the attachment and entry of IAVs. In agreement with a previous study (*36*), the removal of SA completely blocked solo virus infection ($P < 0.001$;

Fig. 3B). AFP-borne viruses continued to infect NA-treated cells by 20 to 59% relative to that without NA treatment ($P < 0.05$), suggesting that AFPs aided the cell entry of loaded viruses independent of the viral receptors.

To further investigate the entry mechanisms of AFP-borne viruses, we used various inhibition modes to hinder the possible cellular uptake pathways, as established previously (*37, 38*). The
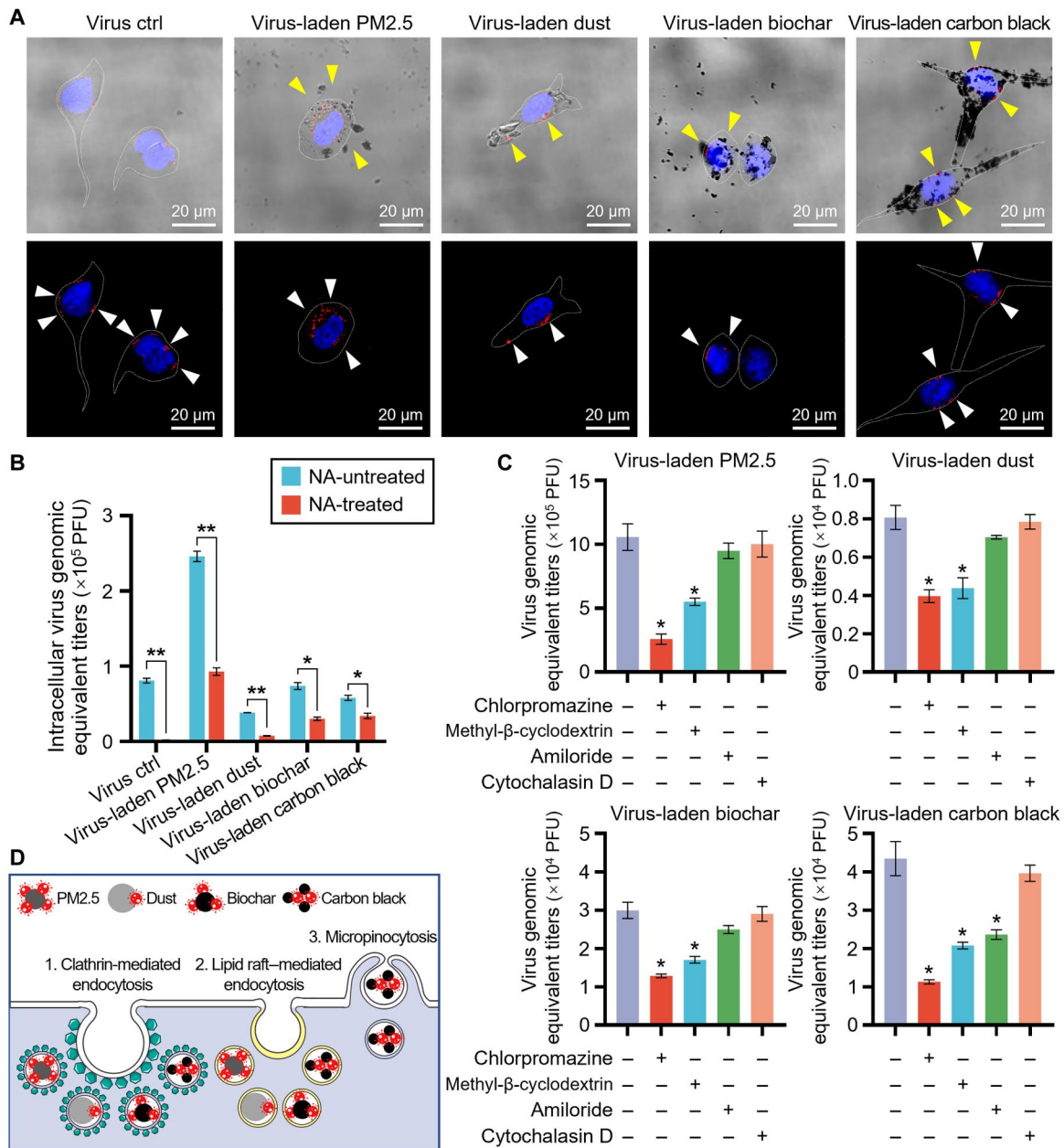
Fig. 3. AFPs transport viruses into target cells. (**A**) Representative merged images of bright-field and fluorescence (top panel) and confocal immunostaining images (bottom panel) of A549 cells upon incubation with solo viruses (at 200 PFU) or virus-laden AFPs (50 µg/ml) for 1 hour. AFPs close to plasma membrane (yellow arrowheads), viruses (white arrowheads), and cell membranes (white dashed lines) are shown. Viral HA protein is stained with an anti-HA antibody (red), and cell nuclei are stained with 4',6-diamidino-2-phenylindole (DAPI; blue). (**B**) Quantification of the replicated viruses in A549 cells with and without neuraminidase (NA) pretreatment following 24 hours of infection with virus-laden AFPs (50 µg/ml; $n = 3$). (**C**) Quantification of replicated viruses in NA-pretreated A549 cells followed by a 24-hour infection with virus-laden AFPs (50 µg/ml) in the presence of different inhibitors ($n = 3$). (**D**) Schematic showing that virus-laden AFPs are mainly internalized through clathrin-dependent endocytosis, followed by lipid raft–mediated endocytosis. *$P < 0.05$; **$P < 0.001$, relative to untreated control, or as indicated.

chlorpromazine treatment decreased by 76% for PM2.5-borne, 51% for dust-borne, 57% for biochar-borne, and 74% for carbon black–borne virus infection, compared to cells without inhibitor treatment ($P < 0.05$; Fig. 3C), suggesting that AFP-borne viruses were internalized primarily by clathrin-mediated endocytosis. Methyl-β-cyclodextrin also significantly repressed viral infection with a weaker effect than chlorpromazine ($P < 0.05$; Fig. 3C), while cytochalasin

D elicited negligible reductions, indicating that virus-laden AFPs were also taken up through lipid raft–mediated endocytosis but not to any degree via macropinocytosis. Carbon black may rely a little more on the micropinocytosis uptake pathway than the other three AFPs ($P < 0.05$; Fig. 3, C and D).

AFPs favor the budding and release of progeny virus

After multiple cycles of viral replication, LSCM imaging revealed that the progeny virions were randomly distributed in the cytoplasm of cells infected with solo viruses, as reported (*31, 34*). Differently in cells infected with AFP-borne viruses, the progeny virions tended to accumulate around AFP localized sites (white arrowheads in Fig. 4A). Lipid rafts have been proved to serve as the preferred sites for viral assembly and budding at the plasma membrane, including for IAVs (*39*), Ebola virus (*40*), herpesviruses (*41*), human respiratory syncytial virus (*42*), and human
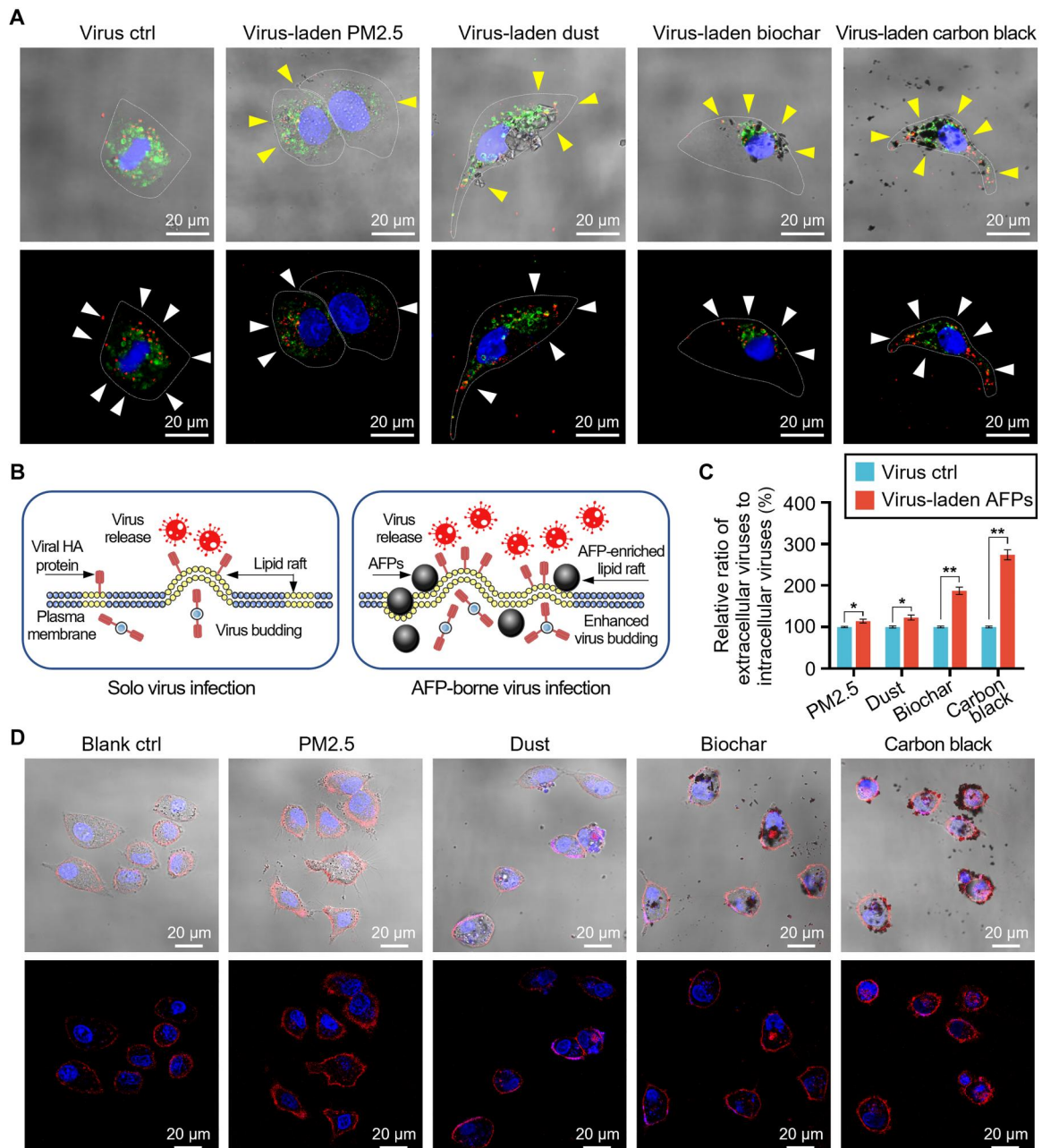

Fig. 4. AFPs favor progeny virion budding. (**A**) Representative merged images of bright-field and fluorescence (top panel) and confocal immunostaining images (bottom panel) of A549 cells upon incubation with solo viruses (at 200 PFU) or virus-laden AFPs (50 μg/ml) for 24 hours. Intracellular virions are stained with an anti-HA antibody (red). Lipid rafts are stained with an anti-flotillin 1 antibody (green). Cell nuclei are stained with DAPI (blue). Yellow arrowheads denote the location of AFPs, and white arrowheads indicate intracellular virions. Cells are indicated through dashed lines. (**B**) Schematic illustrating AFPs in directing the budding and release of progeny virions. (**C**) Relative ratio of extracellular virus counts to intracellular virus counts at 24 hpi (*n* = 4). Virus concentration in virus control is the same as that loaded onto each AFP. Data are presented as percent changes relative to the according virus control. (**D**) Representative merged images of bright-field and fluorescence (top panel) and confocal fluorescence images (bottom panel) of A549 cells treated with AFPs (20 μg/ml) for 24 hours. Red fluorescence (Evans blue) is indicative of the injuries of cell plasma membrane. Cell nuclei are stained with DAPI in blue. *$P < 0.05$; **$P < 0.001$, relative to virus control.

immunodeficiency virus (43). Thus, we performed immunofluorescent staining using an anti-human flotillin 1 antibody (green) to visualize lipid rafts in target cells. The LSCM images showed that lipid rafts were enriched near the AFP-attached plasma membrane and were colocalized with viral HA proteins (Fig. 4A). AFPs, especially the hydrophobic carbon black (fig. S2), bearing a high affinity toward lipids, attached to the plasma membrane and formed lipid raft–enriched domains, whereby the progeny virions were postulated to take advantage of the lipid rafts for apical plasma membrane targeting and budding (Fig. 4B). The mechanism underlying AFP-aided progeny virion budding was also verified in hSAECs (fig. S7).

Furthermore, when the ratio of extracellular to intracellular virus counts was evaluated, we found that PM2.5, dust, biochar, and carbon black enhanced the release of viral progeny by 14, 23, 87, and 174%, respectively, compared to their according virus control groups ($P < 0.05$; Fig. 4C). The larger difference for carbon black compared to the other three AFPs ($P < 0.05$) was consistent with the greater mass of carbon black adsorbed onto the cell plasma membrane, as described in Figs. 3A and 4A. Of note, particles with greater hydrophobicity exhibit higher adsorption capacity onto the plasma membrane (44, 45), and carbon black was the most hydrophobic of the four AFPs (fig. S2), which fundamentally accounted for the highest particle-membrane affinity. Moreover, the injury of host cell membrane has been reported to enhance the release of hepatitis A virus (46), poliovirus (47), and dengue virus (48). On the basis of the principle that dyes tend to accumulate in cells with reduced membrane integrity (49), we looked into the cell plasma membrane injuries upon AFP exposure. In analogy to the above results, all AFPs, particularly carbon black, yielded marked red fluorescence with a three- to sevenfold increase relative to untreated control, indicating active association of these particles with and resultant damage to the plasma membrane ($P < 0.001$; Fig. 4D and fig. S8). Together, our results indicated that AFPs reinforced the intracellular delivery of H1N1 viruses, and the particle-plasma membrane association even favored the budding and release of progeny virions.

AFPs alter H1N1 distribution along the respiratory tract

Afterwards, we further examined the infection of AFP-borne viruses in vivo by administering BALB/c mice with virus-laden AFPs (200 μg/kg body weight) through the intranasal route. This exposure dose of AFPs is equal to about 12 μg/m^3 in ambient air, which is lower than the exposure levels of inhaled particles reported in most studies on the health implications of air pollution (50, 51). Viral titers in the nasal cavity, trachea, and lung corresponding to the upper, middle, and lower respiratory tracts were assessed at 1, 3, and 8 days post infection (dpi) (Fig. 5A). As shown in Fig. 5B, viruses were evenly distributed in the nasal cavity and lung of mice infected with solo viruses at 1 dpi, as reported previously (12, 29). This finding is supported by the spatial expression pattern of specific virus receptors, such as α-2,6 SA-linked receptors, which are more abundant in the lung and nasal cavity than those in the trachea (52, 53). Unlike solo viruses, 82% of PM2.5-borne, 98% of dust-borne, and 76% of biochar-borne viruses that were administered ended up in the lung (Fig. 5B). In contrast, 83% of carbon black–borne viruses still remained in the nasal cavity, with only a small amount reaching the lung at 1 dpi. A similar biodistribution pattern along the airway was identified for Au-doped AFPs that were tracked using inductively coupled

plasma mass spectrometry (Fig. 5C). These results collectively uncovered that different AFP types yielded different viral biodistribution.

In the following, histological examination revealed that particles were visualized to accumulate in the turbinate of nasal cavity from mice upon exposure to virus-laden carbon black (Fig. 5D), but were found in the lung alveoli after exposure to virus-laden PM2.5, dust, and biochar at 1 dpi (black arrowheads in Fig. 5E). Analogously, no particles were readily visualized in the lung after 1 day of exposure to virus-laden carbon black (Fig. 5E), in support of the above results (Fig. 5, B to D). To verify these findings, the virus localization in the lung was also qualitatively and quantitatively corroborated through in situ immunofluorescent staining using an anti-HA antibody (Fig. 5F), which correlated with the virus distribution pattern (Fig. 5B). Among the AFP physicochemical properties, the surface hydrophobicity essentially determined the interaction with and adsorption of AFPs to the plasma membrane (44, 45). Particles with greater hydrophobicity are more easily entrapped and immobilized in the respiratory mucus (54). To this end, carbon black particles were the most hydrophobic of the four AFPs (fig. S2), which contributed to understanding a differential distribution pattern of carbon black along the respiratory tract in comparison to the other three AFPs.

Similar to the reported features of IAV replication (55, 56), viral contents in the lung for solo viruses and all AFP-virus complexes increased rapidly from 1 to 3 dpi before declining steadily between 3 and 8 dpi (Fig. 5F and fig. S9, A and B). Nevertheless, at the terminal point of infection (8 dpi), abundant viruses still remained in the lung (fig. S9B), consistent with the robust replication ability of IAVs in the lower respiratory tract (53). Of note, AFP-borne virus infection still induced greater proportion of virus distribution in the lung than that in the virus control group at 3 and 8 dpi (Fig. 5B). Consequently, sustained inflammatory cell infiltration and histological damage were visualized (fig. S9, A and B).

AFPs function to spread the H1N1 virus to extrapulmonary organs

Although IAV infections largely attack and produce adverse outcomes along the respiratory tract (53, 55, 56), previous studies have shown that respiratory viruses can also reach distant organs and even cause lethal effects (12, 13). Furthermore, we recently unveiled that ^{125}I-radiolabeled AFP particles could enter the circulation from the lung and thereafter accumulate in the liver, spleen, kidney, knee joint, and even the brain (8, 9). Inspired by these findings, we investigated whether AFP-virus complexes also spread to extrapulmonary sites. To realize this, H1N1 PR8 viruses labeled with an anti-HA antibody (green) and red fluorescent SiO$_2$ particles with a similar composition to dust were used.

Whole-mount sections of the lung revealed that solo viruses tended to infect the tracheal epithelial cells (white arrowheads in Fig. 6A) at 1 dpi, as reported previously (56). On their own, SiO$_2$ particles translocated from distal bronchioles into the alveolar parenchyma (Fig. 6A, middle panel), in agreement with our previous reports (8, 9). This intrusion into the interstitial compartment suggested that SiO$_2$ particles could traverse the blood-air barrier (8, 9). Notably, with virus-laden SiO$_2$ particles, we found virus signals (green) overlapping with particle signals (red) in the interstitial compartments (yellow arrowheads in Fig. 6A) and notably also in distant organs including the liver, spleen, and kidney (Fig. 6B).

Fig. 5. AFPs alter the distribution of viruses along the respiratory tract. (**A**) Timeline and experimental design for evaluating viral titers in the nasal cavity, trachea, and lung in BALB/c mice that were intranasally infected with virus-laden AFPs (200 μg/kg body weight). i.n., intranasal. (**B**) Percentage of viruses detected in the nasal cavity (red), trachea (green), and lung (blue) through SYBR green–based qRT-PCR analysis at 1, 3, and 8 days post infection (dpi; $n = 5$). Data are presented as the proportion of virus titers at each site relative to the whole titers in the respiratory tract. (**C**) Inductively coupled plasma mass spectrometry analysis of Au content in the nasal cavity (red), trachea (green), and lung (blue) of mice intranasally administered with 1.0 mg/kg body weight Au-doped AFPs for 2 hours ($n = 4$). Data are presented as the proportion of Au content at each site relative to the whole mass in the respiratory tract. (**D**) Representative nasal cavity sections from mice treated with 1.0 mg/kg body weight virus-laden AFPs for 2 hours. Inserts show magnified views of smaller red squares. Blank control is PBS only. (**E**) Representative hematoxylin and eosin (H&E)–stained lung sections from mice treated with PBS (blank control), solo viruses, or virus-laden AFPs (200 μg/kg body weight) at 1 dpi. AFP accumulation (black arrowheads) is observed. (**F**) Representative confocal images of lung sections obtained from mice as described in (E). Viruses are stained with an anti-HA antibody (green), and cell nuclei are stained with DAPI (blue).
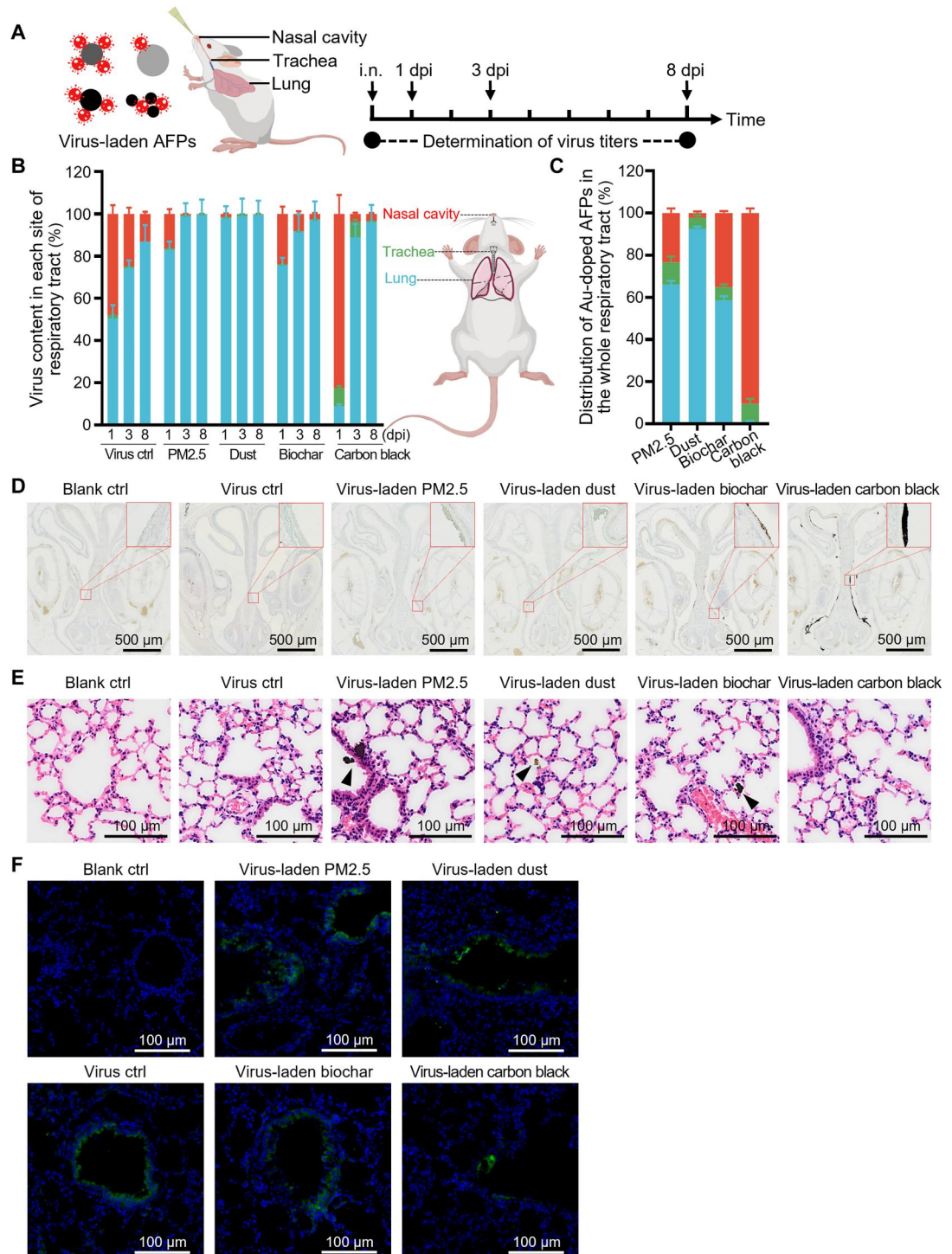
Constant findings were also verified in polystyrene particle–borne virus infection (fig. S10A). In addition, virus localization was validated in these organs from mice upon infections of all AFP-borne viruses using immunofluorescent staining of viral HA protein (fig. S10B). Collectively, these results substantiated that virus-laden AFPs could traverse the blood-air barrier and be transported to extrapulmonary organs through the blood circulation.

To elaborate on how AFPs drive the virus spread following infection, we quantified the viral titers in the blood and distant organs using a more sensitive method via the determination of viral polymerase acidic (*PA*) protein gene by TaqMan qRT-PCR (fig. S10C), as previously reported (*29*). A quick and notable increase of the viral titers was observed in the blood and extrapulmonary organs (liver, spleen, and kidney) following the infection with virus-laden PM2.5,
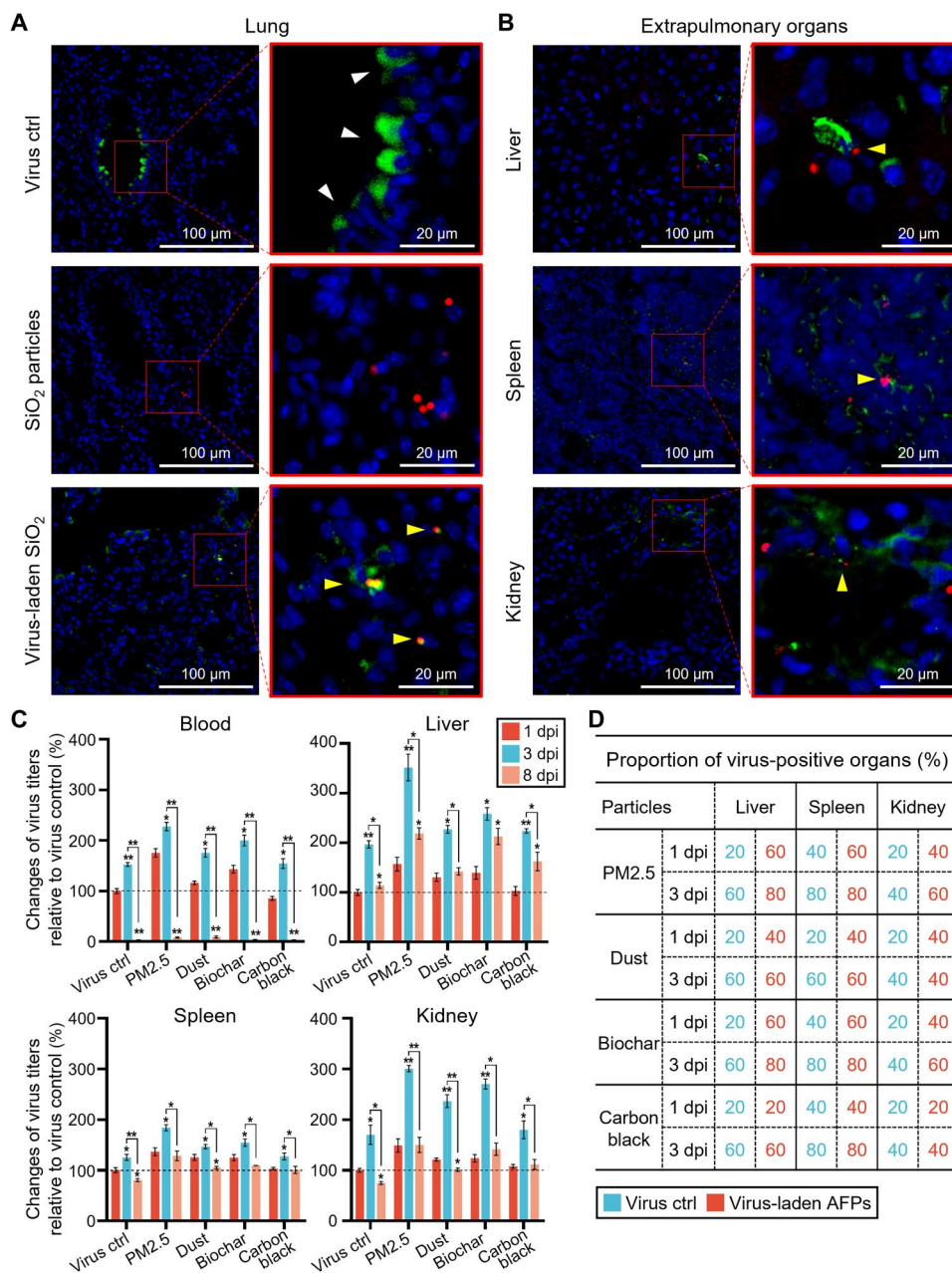
Fig. 6. AFPs drive the spread of viruses into extrapulmonary organs. (**A**) Representative confocal images of lung sections obtained from mice treated with solo viruses (top panel), SiO$_2$ particles (middle panel), or virus-laden SiO$_2$ particles (200 μg/kg body weight; bottom panel) for 1 day. SiO$_2$ control group received the same mass of particles as the virus-laden SiO$_2$ group. Virus concentration in virus control is equal to that loaded onto SiO$_2$ particles. (**B**) Representative immunofluorescent staining of the liver, spleen, and kidney sections obtained from mice treated with virus-laden SiO$_2$ particles for 3 days. The right panel indicates magnified views of red squares. Viruses are stained with an anti-HA antibody (green), and cell nuclei are stained with DAPI (blue). (**C**) Relative changes of virus titers in the blood and distant organs (liver, spleen, and kidney) from mice infected with virus-laden AFPs (200 μg/kg body weight) or solo viruses at 1, 3, and 8 dpi ($n = 5$). Virus titers are quantified through TaqMan qRT-PCR and presented as percent changes relative to the corresponding virus control at 1 dpi. Ct value >38 was considered nondetectable. (**D**) Proportion of virus-positive organs in animals infected with virus-laden AFPs (200 μg/kg body weight) in contrast to the same titers of solo viruses at 1 and 3 dpi, as determined by TaqMan qRT-PCR ($n = 10$). *$P < 0.05$; **$P < 0.001$, relative to the corresponding virus control at 1 dpi, or as indicated.

dust, and biochar at 1 dpi ($P < 0.05$; Fig. 6C). Except for carbon black, it remained in the upper airway and was slower in driving viral extrapulmonary transport (Fig. 6C). Because of the viral transport and replication, virus titers at each site increased rapidly at 3 dpi for AFP-borne virus infection ($P < 0.05$; Fig. 6C). AFP-borne virus infection showed higher proportions (up to threefold) of virus-positive organs than the virus control at 1 and 3 dpi (Fig. 6D). The viral titers markedly dropped to nearly nondetectable levels in the blood at 8 dpi for all infections ($P < 0.001$) but still remained at high levels in the extrapulmonary organs (Fig. 6C). Of note, no virus was detected in the heart and brain in this experiment. These findings suggested that AFPs aided the transport of viruses to extrapulmonary organs.

AFP-borne viruses cause more severe phenotypes than AFPs alone or solo viruses in mice

With these encouraging findings, we looked further into the adverse outcomes both systemically and locally in mice challenged by diverse infections. Neutrophils are rapidly mobilized from the bone marrow upon viral infection, leading to an increase in the peripheral circulation (57). In the presence of inflammatory signals, circulating lymphocytes are recruited to the infected respiratory tract, resulting in lower peripheral counts (58). Thereby, as a classical parameter to assess the inflammatory state in virus infection, the ratio of neutrophil/lymphocyte has been reported to indicate the occurrence, development, and outcomes of infectious diseases (59, 60). In agreement with the accumulation of inflammatory cells in the lung (Fig. 5E and fig. S9), complete blood count analysis validated that PM2.5-, dust-, and biochar-borne viruses induced 44 to 105% increase in the neutrophil counts and 5 to 7% decrease in the lymphocyte counts in the peripheral blood, compared to untreated blank control at 1 dpi ($P < 0.05$; Fig. 7, A to C). Otherwise, carbon black–borne viruses did not induce substantial changes in these parameters early on in the infection (Fig. 7D).

During the later stage of infection, i.e., at 3 and 8 dpi, AFP-borne viruses and solo viruses, especially the former, induced systemic inflammation. We observed a significant increase in neutrophil counts and a significant drop in lymphocyte counts in the AFP-borne virus treatments ($P < 0.001$), while changes in the peripheral blood were marginal in mice treated with AFPs only (Fig. 7, A to D). Consistently, systemic inflammation was more pronounced in PM2.5-borne virus infection than in the other three AFP-borne virus infections ($P < 0.05$; Fig. 7, A to D). Moreover, AFP-borne virus infection resulted in a 14 to 65% increase in the ratio of neutrophil/lymphocyte compared to virus control, indicating that the AFP-virus complex elicited more severe inflammation ($P < 0.05$; Fig. 7, A to D). Notably, because of the enhanced transport of AFP-virus complexes to distant organs, local inflammation was observed in the hematoxylin and eosin (H&E)–stained images of the liver, spleen, and kidney (figs. S11 to S13). Together, these data revealed that AFPs markedly altered biodistribution and provoked inflammatory responses to the viruses in the lung and other sites.

In addition to the observed inflammation, all virus infections caused a marked reduction in body weight, which is one of the common symptoms after IAV infection and is believed to be caused by multiple pathologies, including fever and decreased food/water intake (61, 62). PM2.5-, dust-, and biochar-borne viruses afflicted the infected animals with quick body weight loss at the early stage of infection, with PM2.5 quickly showing the

greatest weight loss ($P < 0.001$; Fig. 7E). However, carbon black–borne viruses displayed delayed body weight loss during 1 to 3 dpi (Fig. 7E). This difference should be ascribed to the retention of carbon black particles in the upper respiratory tract and slower transport into the lung. Overall, our data manifested that AFP-borne virus infections (to a divergent degree) resulted in more marked body weight reduction than their according virus control (Fig. 7E). The more severe phenotypes in animals induced by AFP-borne viruses in comparison to virus alone should reside in (at least partially) the AFP-aided transportation of viruses deep into the lung and on to distant organs, as well as the synergistic toxicities by AFPs and viruses. Together, our results unearthed that, besides acting as a carrier, AFPs could markedly drive the biodistribution and inflammatory responses of the viruses along the respiratory tract and afterwards to the distant sites, inducing detrimental effects that were different from (even more severe than) those produced by AFPs alone or solo viruses.

DISCUSSION

The implication and contribution of airborne particles in pathogen spread and infection have been studied for years. Under realistic exposure scenarios, respiratory viruses are reported to be mostly transported by aerosols and AFPs (6, 7). However, exactly how AFPs interact with viruses and involve in the viral infection process is largely unknown. The previous research mainly focused on the indirect effects of AFPs on viral infection, such as the damage of defense networks against pathogens or the promotion of viral receptor expression (14–18). Despite these progresses, it is crucial to understand the impacts of AFPs per se on virus loading, as well as the influence of AFPs on the viral infection process, including viral entry, replication, and release. Here, four typical AFPs with diverse sources and compositions were selected, comprising naturally sampled PM2.5, silica-based dust, biomass-derived biochar, and fossil fuel–derived carbon black. Under influence of various physicochemical properties, the AFP-virus interactions markedly affected viral lifecycle and tissue distribution and ultimately elicited divergent pathogenesis and outcomes of respiratory infection. For example, AFPs (especially the hydrophobic carbon black) promoted the formation of lipid raft–enriched fractions on the plasma membrane, where the progeny virions targeted and took advantage of the lipid rafts for budding.

The translocation and biodistribution of AFPs have been verified to dictate their toxic effects (10, 11). Recent studies from our and other groups have continued to elaborate on the extrapulmonary translocation of exogenous fine particles (8–11). As evidenced by previous reports, particles with fine size could escape from the body's protection system and reach deep into the alveolus regions of the lung, and then damage and penetrate the air-blood barrier (8, 9). The particles that translocated into the blood circulation could distribute to other secondary organs, including the liver, spleen, and kidney (8–11). Inhaled AFPs have been found in diverse human tissues, such as the blood, heart, and even brain, highlighting the pathway of particle translocation from the bloodstream to distant organs (63, 64). Likewise, not restricted to the respiratory tract, IAV-associated extrapulmonary infection has been identified, particularly for infection with highly pathogenic virus strains (12, 13). In this context, AFPs provide intriguing possibilities to alter the viral biodistribution and the occurrence and progression of IAV
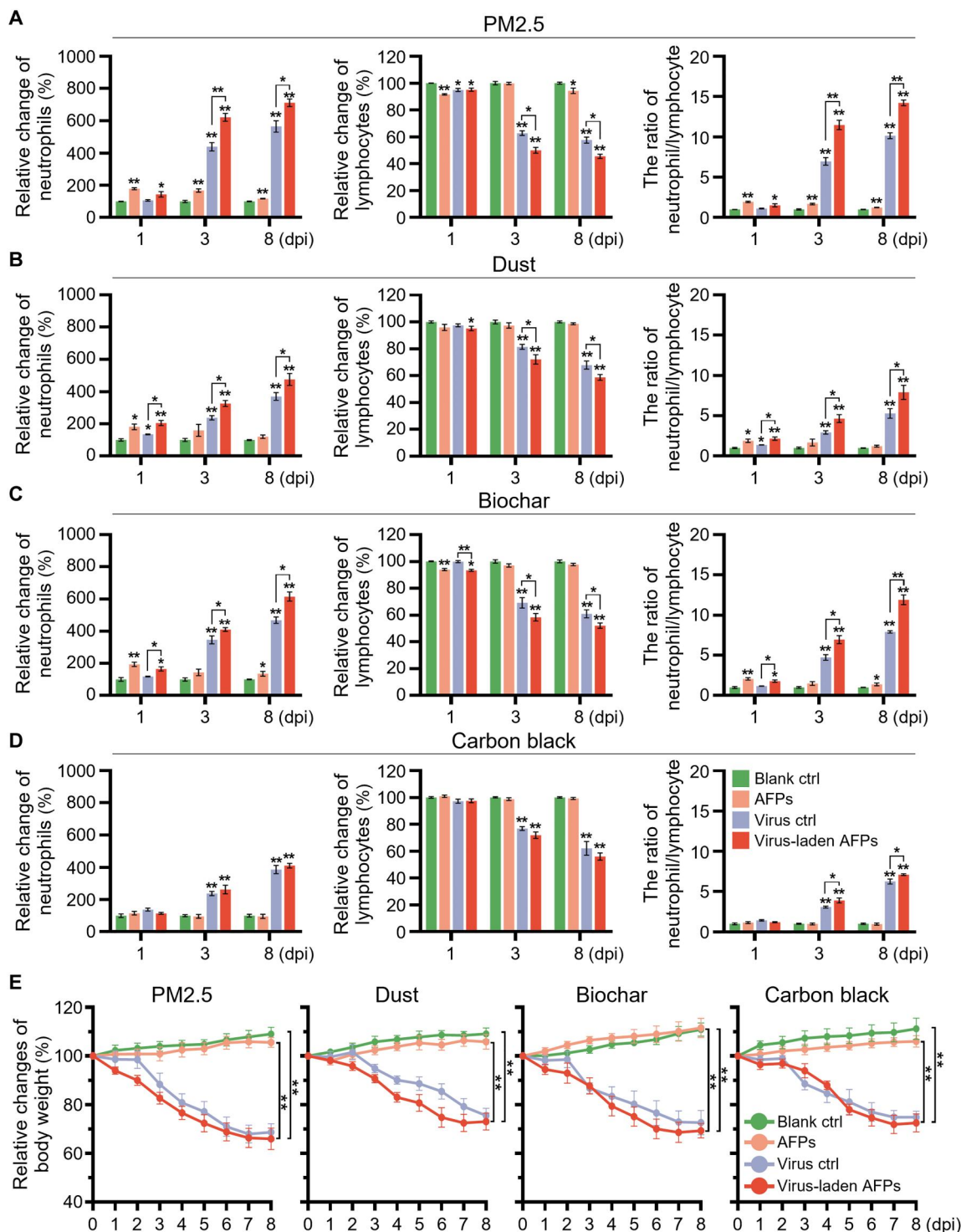
Fig. 7. Virus-laden AFPs cause greater systemic immune responses in vivo than virus infection alone. Relative changes of neutrophil counts (left panel), lymphocyte counts (middle panel), and the ratio of neutrophil/lymphocyte (right panel) in the peripheral blood of mice treated with (**A**) PM2.5-, (**B**) dust-, (**C**) biochar-, and (**D**) carbon black–bearing viruses at 200 μg/kg body weight or the same titers of solo viruses at 1, 3, and 8 dpi (*n* = 5). Change was calculated relative to blank control (PBS). (**E**) Relative changes in body weight of mice treated with PBS (blank control, green line), AFPs alone (orange line), virus control (purple line), and virus-laden AFPs (red line) over the 8-day infection period. Change in body weight was compared with initial weight (*n* = 5 mice per group). Virus titers in virus control are the same as those loaded onto according AFPs. *$P < 0.05$; **$P < 0.001$, relative to blank control, or as indicated.

infection. AFPs could act as a Trojan horse to load viruses and transport them into distant organs. The relatively easier localization of AFP-virus complexes in organs with large-volume blood suggested the tendentious accumulation of particles, as supported by previous findings (*8, 9*). Because of the detrimental health effects, AFP-induced physical damage and immune disorders could reinforce the extrapulmonary translocation of viruses and also hinder viral clearance (*65–67*). Besides, RBCs could be a vehicle to transport both viruses and particles as well (*68, 69*), which was indicated as another potential mechanism in driving the persistent delivery of viruses to distant organs, especially the spleen as the graveyard of RBCs.

In summary, our study uncovered active interactions between AFPs and the H1N1 PR8 virus, which were largely regulated by the physicochemical properties of the AFPs. On the one hand, the surface area and pore volume of the AFPs were the main determinants in governing their virus loading capacity, except for carbon black with a different particle-virus interaction pattern. On the other hand, the surface hydrophobicity of AFPs determined the particle-plasma membrane interactions, resulting in enhanced virus budding and release in target cells and altered viral distribution along the respiratory tract in animals. Notably, we found that AFPs provided a receptor-independent path for viral entry into and budding from host cells. Moreover, these particles drove the loaded viruses deep into the lower respiratory tract and on to distant organs, such as the liver, spleen, and kidney. As a result, AFP-borne viruses (in particular, PM2.5-borne viruses) yielded more severe infection than the virus alone, characterized by local tissue injuries, systemic inflammation, and body weight loss. The overall findings are summarized in Fig. 8. Our results offer detailed insights into the impact of air pollution on respiratory infection, providing further urgency for prioritizing air quality management and air pollution reduction policies.

MATERIALS AND METHODS

Ethics statement
All animal experimental designs and protocols were approved by the Animal Ethics Committee at the Research Center for Eco-Environmental Sciences, Chinese Academy of Sciences. The ethical approval number is AEWC-RCEES-2020001. All virus infection protocols were conducted in strict accordance with the standards of the Institute of Microbiology, Chinese Academy of Sciences.

Viral amplification and quantification
The mouse-adapted human H1N1 PR8 virus and the recombinant H1N1 PR8 virus with *NA* gene segment harboring *EGFP* gene (EGFP-PR8 virus) were respectively propagated and purified, as described previously (*70*). Viral titers were assayed through the plaque assay.

H1N1 PR8 virus and EGFP-PR8 virus were quantified by qRT-PCR analysis. In brief, viral genomic RNAs were extracted via the Viral RNA Rapid Extraction Kit (Zomanbio, China) according to the manufacturer's instructions. Extracted RNAs were reversely transcribed into cDNAs using Script RT All-in-One Mix (Star-Lighter, China). Gene expression levels were determined using an Mx3005P qRT-PCR instrument (Bio-Rad, USA). The primer sequences are listed in table S1.

The standard curves for viral quantitation were generated by a 10-fold serial dilution of virus stocks against the Ct values, with a range from 1.0×10^1 to 1.0×10^7 plaque-forming unit (PFU) viruses for SYBR green–based qRT-PCR analysis, and $1.0 \times 10^{1.7}$ to 1.0×10^6 PFU viruses for TaqMan qRT-PCR analysis. The viral load of each sample was converted using Ct values and the standard curves, as described previously (*29–31*).

Preparation and characterization of AFPs and virus-laden AFPs
PM2.5 samples were collected from Beijing, China. PM2.5 specimens loaded onto the polytetrafluoroethylene filter membranes were eluted in ultrapure water by ultrasonic extraction and then freeze-dried. Dust samples were purchased from the Powder Technology Inc. (USA). Biochar samples were prepared via pyrolyzing biomass from corn straw under oxygen-limited conditions at 500°C, as described previously (*25*). The biochar powder was crushed and passed through a 3-μm sieve. Carbon black samples were purchased from the Degussa Inc. (USA). Red fluorescent SiO₂ particles (with a particle size of 2 μm) and red fluorescent polystyrene particles (with a particle size 2 μm) were purchased from the Baseline Inc. (China). The synthesis and characterization of Au-doped AFPs were performed, as described previously (*8, 9*).

To prepare virus-laden AFPs, AFPs (20, 50, and 100 μg/ml) were coincubated with 1.0×10^4 PFU viruses for 1 hour at room temperature. The mixtures were washed three times with cold phosphate-buffered saline (PBS) by centrifugation at 1000*g* for 6 min to remove any free viruses. The loaded viruses on AFPs were quantified through the SYBR green–based qRT-PCR analysis.

The morphological characteristics of AFPs and virus-laden AFPs were determined by TEM (H-7500, Hitachi, Japan) and SEM (SU-8020, Hitachi, Japan). The size distribution of AFPs was assessed by measuring more than 300 particles in TEM images. The surface area and micropore volume of AFPs were measured via a surface area and porosity analyzer (ASAP2460, Micrometrics, USA). The surface functional groups of AFPs were quantified using an x-ray photoelectron spectrometer (ESCALAB 250Xi, Thermo Fisher Scientific, USA).

The hydrophilicity and hydrophobicity of AFPs were determined using the dye partitioning method. In brief, a series of AFP suspensions at different concentrations were coincubated with NB (20 μg/ml; Sigma-Aldrich, USA) or RB (20 μg/ml; Sigma-Aldrich, USA) solution for 3 hours at room temperature. After centrifugation at 16,000*g* for 1 hour, the NB and RB molecules in the supernatants were recorded at 620 and 549 nm with an ultraviolet-visible spectrometer (Epoch, BioTek, USA). The partitioning quotient (PQ) was calculated by the ratio of the dye bound onto the particle surface (D_{bound}) to free dye molecules in the liquid phase (D_{free}); i.e., $PQ = D_{bound}/D_{free}$. The linear relationship between PQ and AFP surface area was analyzed. The total surface area of the particles dispersed in the suspension was calculated from the hydrodynamic size of these particles determined by the Zetasizer Nano ZS (Malvern Panalytical, UK) with the assumption of a spherical shape, as previously described (*71*).

HA test
To test the viral HA activity, AFPs (50 μg/ml) were first coincubated with 1.0×10^6 PFU viruses for the designed times at room temperature. Then, 50 μl of mixtures were incubated with equal volumes of
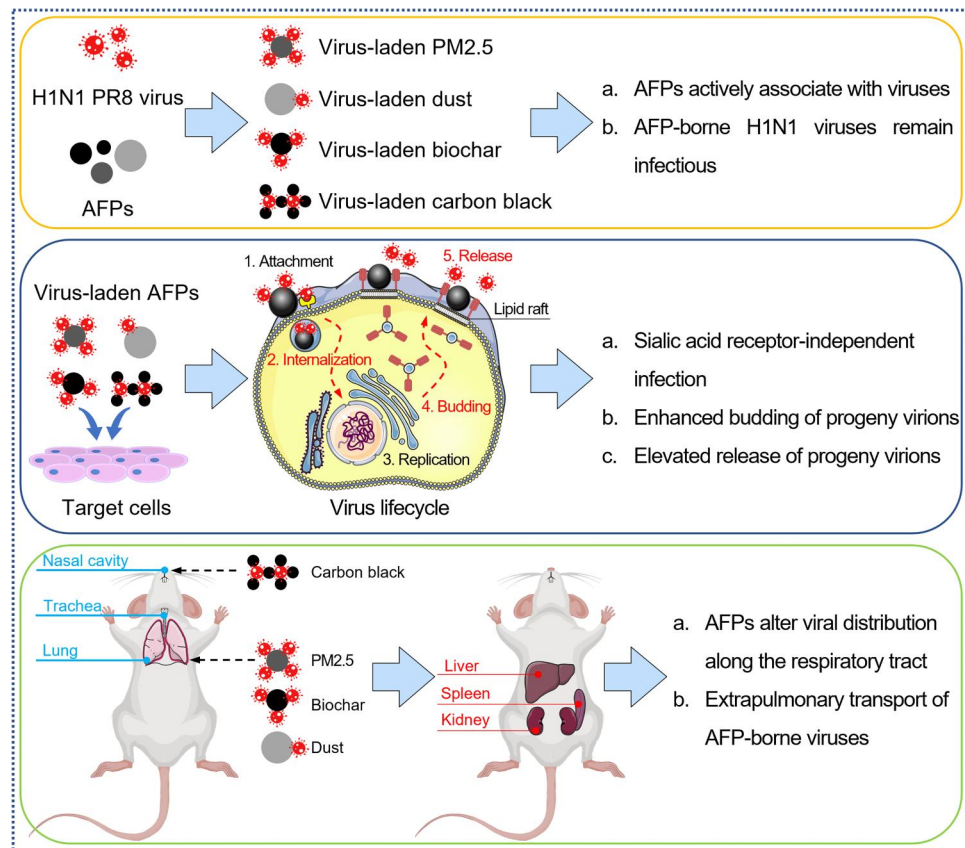
Fig. 8. Schematic illustration of the interaction between AFPs and H1N1 virus and the spread of the virus driven by AFPs. AFPs such as PM2.5, dust, biochar, and carbon black adsorb different amounts of viruses to form infectious AFP-virus complexes (top panel). AFP-virus complexes infect the host cells through a receptor-independent pathway, and AFPs direct the internalization and budding of the viruses (middle panel). Different AFP-borne viruses are distributed at different locations along the respiratory tract and transported into distant extrapulmonary organs (bottom panel).

2% chicken erythrocytes (Beijing Merial Vital Laboratory Animal Technology Co. Ltd., China) for 30 min at room temperature in the V bottom of 96-well plates. High HA activity occurs when viral HA protein cross-links with RBCs and forms a diffuse reddish solution. RBCs precipitate at the bottom of the well when few or no viruses bind to them. Agglutinated erythrocytes were quantified by examining the absorbance of hemoglobin at 575 nm using a plate reader (Thermo Fisher Scientific, USA). The same amounts of viruses were used as the virus control.

Cell culture
A549 cells and MDCK cells were purchased from the Shanghai Cell Bank of Type Culture Collection (China) and were cultured in Dulbecco's modified Eagle's medium (DMEM) (Corning, USA) supplemented with 10% fetal bovine serum (NEWZERUM, New Zealand) and 1% penicillin/streptomycin (Gibco, USA) in a cell incubator with 5% CO_2 and at 37°C. hSAECs were purchased from the iCell Bioscience Inc. (China) and cultured in an airway epithelial cell basal medium according to the manufacturer's protocol.

Cell membrane integrity assay
To assay the membrane permeability, cells were treated with AFPs (20 μg/ml) for 24 hours and stained with a cell membrane integrity assay kit, following the manufacturer's protocol (BestBio Biotechnology Co. Ltd., China).

Plaque assay
To test the titers of virus stock, MDCK cells in confluent monolayers were infected with 10-fold serially diluted viruses. To evaluate the infectivity of viruses, cells were incubated with virus-laden AFPs (20, 50, and 100 μg/ml) or solo viruses. After the infection at 37°C for 1 hour, cells were overlaid with DMEM supplemented with 1% low melting agarose (GenStar, China), 1% bovine serum albumin (Solarbio, China) and [N-tosyl-L-phenylalanyl chloromethyl ketone]–treated trypsin (1 μg/ml; Sigma-Aldrich, USA). At 48 hpi, cells were stained with 0.25% crystal violet solution (Solarbio, China), following fixing with 4% paraformaldehyde (Biorigin, China). Viral titers or infectivity were determined by the number of plaques.

Viral infection of pulmonary epithelial cells
For viral internalization assay, target cells were incubated with virus-laden AFPs (50 μg/ml) or solo viruses at 37°C for 1 hour. To investigate viral replication and release, cells were further cultured for 8, 24, and 48 hours. To verify the receptor-independent infection pattern of AFP-borne viruses, cells were treated with

NA enzyme (1 U/ml; Solarbio, China) at 37°C for 2 hours, followed by infection for 24 hours.

To investigate the uptake mechanism of virus-laden AFPs, cells were pretreated with NA enzyme (1 U/ml) at 37°C for 2 hours and immediately incubated with diverse inhibitors in complete cell culture medium at 37°C for 1 hour, followed by infection with virus-laden AFPs (50 μg/ml) for 24 hours. Chlorpromazine (5 μg/ml; Solarbio, China) was used to inhibit clathrin-mediated endocytosis; methyl-β-cyclodextrin (20 μg/ml; Macklin Biochemical Co. Ltd., China) was used to inhibit lipid raft–mediated endocytosis; amiloride (50 μg/ml; Solarbio, China) was used to block micropinocytosis; cytochalasin D (2.5 μg/ml; Aladdin Biochemical Technology Co. Ltd., China) was used to inhibit actin polymerization and macropinocytosis, as established previously (37, 38).

Intracellular viruses were quantified via SYBR green–based qRT-PCR analysis following the extraction of total cellular RNAs, and progeny viruses in the corresponding culture medium were quantified according to the procedure of viral quantification.

Flow cytometry analysis
Target cells were infected with EGFP-PR8 virus-laden AFPs or solo viruses for 8, 24, and 48 hours. Afterwards, live cells were distinguished using the Fixable Viability Dye 780 (Thermo Fisher Scientific, USA) staining assay. The percentage of EGFP-positive cells within gated Fixable Viability Dye–negative cells was determined with Attune NxT Flow Cytometer (Thermo Fisher Scientific, USA).

Immunofluorescence assay
Target cells were infected with AFP-borne viruses or solo viruses and then were extensively washed with PBS and fixed with methanol for 15 min at −20°C. After washing, these cell specimens were blocked with blocking buffer (PBS containing 5% goat serum and 0.3% Triton X-100) for 1 hour at room temperature, and further incubated with mouse monoclonal anti-HA antibody (1:200; Abcam, UK) and/or rabbit monoclonal anti-flotillin 1 antibody (1:500; Abcam, UK) at 4°C overnight. Cells were sequentially stained with CoraLite 594–conjugated goat anti-mouse immunoglobulin G (IgG; 1:500; ProteinTech, USA) and/or fluorescein isothiocyanate–conjugated goat anti-rabbit IgG (1:500; ProteinTech, USA) for 1 hour, followed by staining with 4′,6-diamidino-2-phenylindole (DAPI; 1 μg/ml; Thermo Fisher Scientific, USA) for 15 min at room temperature. After thoroughly washing, fluorescent signals were visualized through LSCM (Leica, Germany).

Animal experimentation
Seven-week-old female BALB/c mice were purchased from the Vital River Laboratory Animal Technology Co. Ltd. (Beijing, China) and were cared and bred in the biosafety level 2 facility at the Institute of Microbiology, Chinese Academy of Sciences. Mice were intranasally administrated with virus-laden AFPs or solo viruses after being anesthetized by pentobarbital sodium. For in situ fluorescence imaging, mice were intranasally administered with virus-laden SiO_2 particles or virus-laden polystyrene particles, and the frozen sections of organs were prepared and examined at 1, 3, and 8 dpi. Solo viruses and particles alone served as controls.

Peripheral blood was analyzed with a hematology analyzer (Nihon Kohden, Japan). Viral titers in the blood, nasal cavity, trachea, lung, liver, spleen kidney, brain, and heart were quantified via qRT-PCR analysis following the extraction of total tissue RNAs.

H&E staining of various tissues was performed following the standard protocols (72, 73). For the immunofluorescence assay, frozen sections of the diverse tissues were prepared, and the viruses were visualized with an anti-HA antibody (1:200; Abcam, UK). All sections were scanned by a digital slide scanner (KFBIO, China).

Statistical analysis
Experimental results were presented as the means ± standard error of the mean. Statistical analysis was assessed with the independent t test or one-way analysis of variance (ANOVA) test using GraphPad Prism 8 software and Statistical Package for the Social Sciences software. In the current study, P values ($P < 0.05$ and $P < 0.001$) define the level of statistical significance.

REFRENCES AND NOTES

1. G. Chen, W. Zhang, S. Li, Y. Zhang, G. Williams, R. Huxley, H. Ren, W. Cao, Y. Guo, The impact of ambient fine particles on influenza transmission and the modification effects of temperature in China: A multi-city study. *Environ. Int.* **98**, 82–88 (2017).

2. X. Wu, R. C. Nethery, M. B. Sabath, D. Braun, F. Dominici, Air pollution and COVID-19 mortality in the United States: Strengths and limitations of an ecological regression analysis. *Sci. Adv.* **6**, eabd4049 (2020).

3. M. Kogevinas, G. Castaño-Vinyals, M. Karachaliou, A. Espinosa, R. de Cid, J. Garcia-Aymerich, A. Carreras, B. Cortés, V. Pleguezuelos, A. Jiménez, M. Vidal, C. O'Callaghan-Gordo, M. Cirach, R. Santano, D. Barrios, L. Puyol, R. Rubio, L. Izquierdo, M. Nieuwenhuijsen, P. Dadvand, R. Aguilar, G. Moncunill, C. Dobaño, C. Tonne, Ambient air pollution in relation to SARS-CoV-2 infection, antibody response, and COVID-19 disease: A cohort study in Catalonia, Spain (COVICAT Study). *Environ. Health Perspect.* **129**, 117003 (2021).

4. M. Dolci, C. Favero, V. Bollati, L. Campo, A. Cattaneo, M. Bonzini, S. Villani, R. Ticozzi, P. Ferrante, S. Delbue, Particulate matter exposure increases JC polyomavirus replication in the human host. *Environ. Pollut.* **241**, 234–239 (2018).

5. S. J. K. Hussey, J. Purves, N. Allcock, V. E. Fernandes, P. S. Monks, J. M. Ketley, P. W. Andrew, J. A. Morrissey, Air pollution alters *Staphylococcus aureus* and *Streptococcus pneumoniae* biofilms, antibiotic tolerance and colonisation. *Environ. Microbiol.* **19**, 1868–1880 (2017).

6. S. Asadi, N. G. B. Hnia, R. S. Barre, A. S. Wexler, W. D. Ristenpart, N. M. Bouvier, Influenza A virus is transmissible via aerosolized fomites. *Nat. Commun.* **11**, 4062 (2020).

7. J. Zhou, J. Wei, K. T. Choy, S. F. Sia, D. K. Rowlands, D. Yu, C. Y. Wu, W. G. Lindsley, B. J. Cowling, J. McDevitt, M. Peiris, Y. Li, H. L. Yen, Defining the sizes of airborne particles that mediate influenza transmission in ferrets. *Proc. Natl. Acad. Sci. U.S.A.* **115**, E2386–E2392 (2018).

8. Y. Qi, S. Wei, T. Xin, C. Huang, Y. Pu, J. Ma, C. Zhang, Y. Liu, I. Lynch, S. Liu, Passage of exogenous fine particles from the lung into the brain in humans and animals. *Proc. Natl. Acad. Sci. U.S.A.* **119**, e2117083119 (2022).

9. Y. Qi, S. Wei, Y. Chen, Y. Pu, S. Liu, Y. Liu, Intrusion of inhaled exotic ultrafine particles into the knee joint in humans and animals: A risk to the joint and surrounding tissues. *Nano Today* **43**, 101426 (2022).

10. B. A. Maher, I. A. M. Ahmed, V. Karloukovski, D. A. MacLaren, P. G. Foulds, D. Allsop, D. M. A. Mann, R. Torres-Jardón, L. Calderon-Garciduenas, Magnetite pollution nanoparticles in the human brain. *Proc. Natl. Acad. Sci. U.S.A.* **113**, 10797–10801 (2016).

11. D. Lu, Q. Luo, R. Chen, Y. Zhuansun, J. Jiang, W. Wang, X. Yang, L. Zhang, X. Liu, F. Li, Q. Liu, G. Jiang, Chemical multi-fingerprinting of exogenous ultrafine particles in human serum and pleural effusion. *Nat. Commun.* **11**, 2567 (2020).

12. M. Imai, T. Watanabe, M. Kiso, N. Nakajima, S. Yamayoshi, K. Iwatsuki-Horimoto, M. Hatta, S. Yamada, M. Ito, Y. Sakai-Tagawa, M. Shirakura, E. Takashita, S. Fujisaki, R. McBride, A. J. Thompson, K. Takahashi, T. Maemura, H. Mitake, S. Chiba, G. Zhong, S. Fan, K. Oishi, A. Yasuhara, K. Takada, T. Nakao, S. Fukuyama, M. Yamashita, T. J. S. Lopes, G. Neumann, T. Odagiri, S. Watanabe, Y. Shu, J. C. Paulson, H. Hasegawa, Y. Kawaoka, A highly pathogenic

avian H7N9 influenza virus isolated from a human is lethal in some ferrets infected via respiratory droplets. *Cell Host Microbe* **22**, 615–626.e8 (2017).

13. J. Gu, Z. Xie, Z. Gao, J. Liu, C. Korteweg, J. Ye, L. T. Lau, J. Lu, Z. Gao, B. Zhang, M. A. McNutt, M. Lu, V. M. Anderson, E. Gong, A. C. H. Yu, W. I. Lipkin, H5N1 infection of the respiratory tract and beyond: A molecular pathology study. *Lancet* **370**, 1137–1145 (2007).

14. R. Mishra, P. Krishnamoorthy, S. Gangamma, A. A. Raut, H. Kumar, Particulate matter (PM(10)) enhances RNA virus infection through modulation of innate immune responses. *Environ. Pollut.* **266**, 115148 (2020).

15. A. Kumar, V. S. Patel, J. N. Harding, D. You, S. A. Cormier, Exposure to combustion derived particulate matter exacerbates influenza infection in neonatal mice by inhibiting IL22 production. *Part. Fibre Toxicol.* **18**, 43 (2021).

16. E. Nozza, S. Valentini, G. Melzi, R. Vecchi, E. Corsini, Advances on the immunotoxicity of outdoor particulate matter: A focus on physical and chemical properties and respiratory defence mechanisms. *Sci. Total Environ.* **780**, 146391 (2021).

17. J. C. Smith, E. L. Sausville, V. Girish, M. L. Yuan, A. Vasudevan, K. M. John, J. M. Sheltzer, Cigarette smoke exposure and inflammatory signaling increase the expression of the SARS-CoV-2 receptor ACE2 in the respiratory tract. *Dev. Cell* **53**, 514–529.e3 (2020).

18. X. Jin, J. Zhang, Y. Li, Z. Zhang, T. Cui, Y. Wang, L. Yao, X. Yang, G. Qu, Y. Zheng, G. Jiang, Exogenous chemical exposure increased transcription levels of the host virus receptor involving coronavirus infection. *Environ. Sci. Technol.* **56**, 1854–1863 (2022).

19. T. Fang, L. Zeng, D. Gao, V. Verma, A. B. Stefaniak, R. J. Weber, Ambient size distributions and lung deposition of aerosol dithiothreitol-measured oxidative potential: Contrast between soluble and insoluble particles. *Environ. Sci. Technol.* **51**, 6802–6811 (2017).

20. K. Ram, R. C. Thakur, D. K. Singh, K. Kawamura, A. Shimouchi, Y. Sekine, H. Nishimura, S. K. Singh, C. M. Pavuluri, R. S. Singh, S. N. Tripathi, Why airborne transmission hasn't been conclusive in case of COVID-19? An atmospheric science perspective. *Sci. Total Environ.* **773**, 145525 (2021).

21. A. Ishmatov, "SARS-CoV-2 is transmitted by particulate air pollution": Misinterpretations of statistical data, skewed citation practices, and misuse of specific terminology spreading the misconception. *Environ. Res.* **204**, 112116 (2022).

22. X. Liu, W. Wei, Z. Liu, E. Song, J. Lou, L. Feng, R. Huang, C. Chen, P. C. Ke, Y. Song, Serum apolipoprotein A-I depletion is causative to silica nanoparticles-induced cardiovascular damage. *Proc. Natl. Acad. Sci. U.S.A.* **118**, e2108131118 (2021).

23. P. S. Chen, F. T. Tsai, C. K. Lin, C. Y. Yang, C. C. Chan, C. Y. Young, C. H. Lee, Ambient influenza and avian influenza virus during dust storm days and background days. *Environ. Health Perspect.* **118**, 1211–1216 (2010).

24. X. Zhou, K. Josey, L. Kamareddine, M. C. Caine, T. Liu, L. J. Mickley, M. Cooper, F. Dominici, Excess of COVID-19 cases and deaths due to fine particulate matter exposure during the 2020 wildfires in the United States. *Sci. Adv.* **7**, eabi8789 (2021).

25. J. Ma, X. Liu, Y. Yang, J. Qiu, Z. Dong, Q. Ren, Y. Y. Zuo, T. Xia, W. Chen, S. Liu, Binding of benzo[a]pyrene alters the bioreactivity of fine biochar particles toward macrophages leading to deregulated macrophagic defense and autophagy. *ACS Nano* **15**, 9717–9731 (2021).

26. Y. Lin, X. Huang, Y. Liu, D. Cao, D. Lu, Z. Feng, Q. Liu, Z. Lin, G. Jiang, Identification, quantification, and imaging of the biodistribution of soot particles by mass spectral fingerprinting. *Anal. Chem.* **93**, 6665–6672 (2021).

27. Y. Wu, Y. Guo, H. Song, W. Liu, Y. Yang, Y. Liu, N. Sang, Y. Y. Zuo, S. Liu, Oxygen content determines the bio-reactivity and toxicity profiles of carbon black particles. *Ecotoxicol. Environ. Saf.* **150**, 207–214 (2018).

28. T. Noda, Native morphology of influenza virions. *Front. Microbiol.* **2**, 269 (2011).

29. H. Achdout, E. B. Vitner, B. Politi, S. Melamed, Y. Yahalom-Ronen, H. Tamir, N. Erez, R. Avraham, S. Weiss, L. Cherry, E. Bar-Haim, E. Makdasi, D. Gur, M. Aftalion, T. Chitlaru, Y. Vagima, N. Paran, T. Israely, Increased lethality in influenza and SARS-CoV-2 coinfection is prevented by influenza immunity but not SARS-CoV-2 immunity. *Nat. Commun.* **12**, 5819 (2021).

30. T. Frensing, S. Y. Kupke, M. Bachmann, S. Fritzsche, L. E. Gallo-Ramirez, U. Reichl, Influenza virus intracellular replication dynamics, release kinetics, and particle morphology during propagation in MDCK cells. *Appl. Microbiol. Biotechnol.* **100**, 7181–7192 (2016).

31. M. I. Goncheva, C. Conceicao, S. W. Tuffs, H. M. Lee, M. Quigg-Nicol, I. Bennet, F. Sargison, A. C. Pickering, S. Hussain, A. C. Gill, B. M. Dutia, P. Digard, J. R. Fitzgerald, *Staphylococcus aureus* lipase 1 enhances influenza A virus replication. *mBio* **11**, 10.1128/mBio.00975-20, (2020).

32. C. Li, M. Hatta, D. F. Burke, J. Ping, Y. Zhang, M. Ozawa, A. S. Taft, S. C. Das, A. P. Hanson, J. Song, M. Imai, P. R. Wilker, T. Watanabe, S. Watanabe, M. Ito, K. Iwatsuki-Horimoto, C. A. Russell, S. L. James, E. Skepner, E. A. Maher, G. Neumann, A. I. Klimov, A. Kelso, J. McCauley, D. Wang, Y. Shu, T. Odagiri, M. Tashiro, X. Xu, D. E. Wentworth, J. M. Katz, N. J. Cox, D. J. Smith, Y. Kawaoka, Selection of antigenically advanced variants of seasonal influenza viruses. *Nat. Microbiol.* **1**, 16058 (2016).

33. A. B. Russell, C. Trapnell, J. D. Bloom, Extreme heterogeneity of influenza virus infection in single cells. *eLife* **7**, e32303 (2018).

34. Y. M. Liu, M. Shahed-Al-Mahmud, X. Chen, T. H. Chen, K. S. Liao, J. M. Lo, Y. M. Wu, M. C. Ho, C. Y. Wu, C. H. Wong, J. T. Jan, C. Ma, A carbohydrate-binding protein from the edible lablab beans effectively blocks the infections of influenza viruses and SARS-CoV-2. *Cell Rep.* **32**, 108016 (2020).

35. S. Thiele, S. Stanelle-Bertram, S. Beck, N. M. Kouassi, M. Zickler, M. Müller, B. Tuku, P. Resa-Infante, D. van Riel, M. Alawi, T. Günther, F. Rother, S. Hügel, S. Reimering, A. McHardy, A. Grundhoff, W. Brune, A. Osterhaus, M. Bader, E. Hartmann, G. Gabriel, Cellular importin-α3 expression dynamics in the lung regulate antiviral response pathways against influenza A virus infection. *Cell Rep.* **31**, 107549 (2020).

36. Y. Liu, J. Sheng, J. Baggen, G. Meng, C. Xiao, H. J. Thibaut, F. J. M. van Kuppeveld, M. G. Rossmann, Sialic acid-dependent cell entry of human enterovirus D68. *Nat. Commun.* **6**, 8865 (2015).

37. Y. Rui, D. R. Wilson, J. Choi, M. Varanasi, K. Sanders, J. Karlsson, M. Lim, J. J. Green, Carboxylated branched poly(β-amino ester) nanoparticles enable robust cytosolic protein delivery and CRISPR-Cas9 gene editing. *Sci. Adv.* **5**, eaay3255 (2019).

38. S. Lim, W. J. Kim, Y. H. Kim, S. Lee, J. H. Koo, J. A. Lee, H. Yoon, D. H. Kim, H. J. Park, H. M. Kim, H. G. Lee, J. Yun Kim, J. U. Lee, J. Hun Shin, L. Kyun Kim, J. Doh, H. Kim, S. K. Lee, A. L. M. Bothwell, M. Suh, J. M. Choi, dNP2 is a blood-brain barrier-permeable peptide enabling ctCTLA-4 protein delivery to ameliorate experimental autoimmune encephalomyelitis. *Nat. Commun.* **6**, 8244 (2015).

39. T. Ohkura, F. Momose, R. Ichikawa, K. Takeuchi, Y. Morikawa, Influenza A virus hemagglutinin and neuraminidase mutually accelerate their apical targeting through clustering of lipid rafts. *J. Virol.* **88**, 10039–10055 (2014).

40. R. G. Panchal, G. Ruthel, T. A. Kenny, G. H. Kallstrom, D. Lane, S. S. Badie, L. Li, S. Bavari, M. J. Aman, In vivo oligomerization and raft localization of Ebola virus protein VP40 during vesicular budding. *Proc. Natl. Acad. Sci. U.S.A.* **100**, 15936–15941 (2003).

41. X. Wang, N. Zhu, W. Li, F. Zhu, Y. Wang, Y. Yuan, Mono-ubiquitylated ORF45 mediates association of KSHV particles with internal lipid rafts for viral assembly and egress. *PLOS Pathog.* **11**, e1005332 (2015).

42. T. H. Chang, J. Segovia, A. Sabbah, V. Mgbemena, S. Bose, Cholesterol-rich lipid rafts are required for release of infectious human respiratory syncytial virus particles. *Virology* **422**, 205–213 (2012).

43. D. H. Nguyen, J. E. Hildreth, Evidence for budding of human immunodeficiency virus type 1 selectively from glycolipid-enriched membrane lipid rafts. *J. Virol.* **74**, 3264–3272 (2000).

44. M. Daniel, J. Řezníčková, M. Handl, A. Iglič, V. Kralj-Iglič, Clustering and separation of hydrophobic nanoparticles in lipid bilayer explained by membrane mechanics. *Sci. Rep.* **8**, 10810 (2018).

45. R. P. Valle, C. L. Huang, J. S. C. Loo, Y. Y. Zuo, Increasing hydrophobicity of nanoparticles intensifies lung surfactant film inhibition and particle retention. *ACS Sustainable Chem. Eng.* **2**, 1574–1580 (2014).

46. Z. Feng, L. Hensley, K. L. McKnight, F. Hu, V. Madden, L. Ping, S.-H. Jeong, C. Walker, R. E. Lanford, S. M. Lemon, A pathogenic picornavirus acquires an envelope by hijacking cellular membranes. *Nature* **496**, 367–371 (2013).

47. Y.-H. Chen, W. Du, M. C. Hagemeijer, P. M. Takvorian, C. Pau, A. Cali, C. A. Brantner, E. S. Stempinski, P. S. Connelly, H.-C. Ma, P. Jiang, E. Wimmer, G. Altan-Bonnet, N. Altan-Bonnet, Phosphatidylserine vesicles enable efficient en bloc transmission of enteroviruses. *Cell* **160**, 619–630 (2015).

48. P. R. Beatty, H. Puerta-Guardo, S. S. Killingbeck, D. R. Glasner, K. Hopkins, E. Harris, Dengue virus NS1 triggers endothelial permeability and vascular leak that is prevented by NS1 vaccination. *Sci. Transl. Med.* **7**, 304ra141 (2015).

49. Y. Yuan, M. Yin, L. Chen, F. Liu, M. Chen, F. Zhong, Effect of calcium ions on the freeze-drying survival of probiotic encapsulated in sodium alginate. *Food Hydrocoll.* **130**, 107668 (2022).

50. Q. Xing, M. Wu, R. Chen, G. Liang, H. Duan, S. Li, Y. Wang, L. Wang, C. An, G. Qin, N. Sang, Comparative studies on regional variations in PM2.5 in the induction of myocardial hypertrophy in mice. *Sci. Total Environ.* **775**, 145179 (2021).

51. Z. He, H. Zhang, Y. Song, Z. Yang, Z. Cai, Exposure to ambient fine particulate matter impedes the function of spleen in the mouse metabolism of high-fat diet. *J. Hazard. Mater.* **423**, 127129 (2022).

52. Z. Y. Ning, M. Y. Luo, W. B. Qi, B. Yu, P. R. Jiao, M. Liao, Detection of expression of influenza virus receptors in tissues of BALB/c mice by histochemistry. *Vet. Res. Commun.* **33**, 895–903 (2009).

53. J. V. Camp, U. Bagci, Y. K. Chu, B. Squier, M. Fraig, S. M. Uriarte, H. Guo, D. J. Mollura, C. B. Jonsson, Lower respiratory tract infection of the ferret by 2009 H1N1 pandemic influenza A virus triggers biphasic, systemic, and local recruitment of neutrophils. *J. Virol.* **89**, 8733–8748 (2015).

54. Y. Guo, Y. Ma, X. Chen, M. Li, X. Ma, G. Cheng, C. Xue, Y. Y. Zuo, B. Sun, Mucus penetration of surface-engineered nanoparticles in various pH microenvironments. *ACS Nano* **17**, 2813–2828 (2023).

55. J. Zhang, J. Liu, Y. Yuan, F. Huang, R. Ma, B. Luo, Z. Xi, T. Pan, B. Liu, Y. Zhang, X. Zhang, Y. Luo, J. Wang, M. Zhao, G. Lu, K. Deng, H. Zhang, Two waves of pro-inflammatory factors are released during the influenza A virus (IAV)-driven pulmonary immunopathogenesis. *PLOS Pathog.* **16**, e1008334 (2020).

56. Y. Steuerman, M. Cohen, N. Peshes-Yaloz, L. Valadarsky, O. Cohn, E. David, A. Frishberg, L. Mayo, E. Bacharach, I. Amit, I. Gat-Viks, Dissection of influenza infection in vivo by single-cell RNA sequencing. *Cell Syst.* **6**, 679–691.e4 (2018).

57. K. Lim, Y.-M. Hyun, K. Lambert-Emo, T. Capece, S. Bae, R. Miller, D. J. Topham, M. Kim, Neutrophil trails guide influenza-specific CD8⁺ T cells in the airways. *Science* **349**, aaa4352 (2015).

58. P. A. Mudd, J. C. Crawford, J. S. Turner, A. Souquette, D. Reynolds, D. Bender, J. P. Bosanquet, N. J. Anand, D. A. Striker, R. S. Martin, A. C. M. Boon, S. L. House, K. E. Remy, R. S. Hotchkiss, R. M. Presti, J. A. O'Halloran, W. G. Powderly, P. G. Thomas, A. H. Ellebedy, Distinct inflammatory profiles distinguish COVID-19 from influenza with limited contributions from cytokine storm. *Sci. Adv.* **6**, eabe3024 (2020).

59. C. D. Russell, A. Parajuli, H. J. Gale, N. S. Bulteel, P. Schuetz, C. P. C. de Jager, A. J. M. Loonen, G. I. Merekoulias, J. K. Baillie, The utility of peripheral blood leucocyte ratios as biomarkers in infectious diseases: A systematic review and meta-analysis. *J. Infect.* **78**, 339–348 (2019).

60. M. Kala, S. Ahmad, M. Dhebane, K. Das, M. Raturi, M. Tyagi, A. Kusum, A cross-sectional comparative characterization of hematological changes in patients with COVID-19 infection, non-COVID influenza-like illnesses and healthy controls. *Viruses* **15**, 134 (2023).

61. H. T. Groves, S. L. Higham, M. F. Moffatt, M. J. Cox, J. S. Tregoning, Respiratory viral infection alters the gut microbiota by inducing inappetence. *mBio* **11**, e03236-19 (2020).

62. A. Wang, S. C. Huen, H. H. Luan, S. Yu, C. Zhang, J. D. Gallezot, C. J. Booth, R. Medzhitov, Opposing effects of fasting metabolism on tissue tolerance in bacterial and viral inflammation. *Cell* **166**, 1512–1525.e12 (2016).

63. L. Calderon-Garciduenas, A. Gonzalez-Maciel, P. S. Mukherjee, B. Reynoso-Robles, B. Perez-Guille, C. Gayosso-Chavez, R. Torres-Jardon, J. V. Cross, I. A. M. Ahmed, V. V. Karloukovski, B. A. Maher, Combustion- and friction-derived magnetic air pollution nanoparticles in human hearts. *Environ. Res.* **176**, 108567 (2019).

64. W. Wang, Y. Lin, H. Yang, W. Ling, L. Liu, W. Zhang, D. Lu, Q. Liu, G. Jiang, Internal exposure and distribution of airborne fine particles in the human body: Methodology, current understandings, and research needs. *Environ. Sci. Technol.* **56**, 6857–6869 (2022).

65. A. Purkayastha, C. Sen, G. Garcia Jr., J. Langerman, D. W. Shia, L. K. Meneses, P. Vijayaraj, A. Durra, C. R. Koloff, D. R. Freund, J. Chi, T. M. Rickabaugh, A. Mulay, B. Konda, M. S. Sim, B. R. Stripp, K. Plath, V. Arumugaswami, B. N. Gomperts, Direct exposure to SARS-CoV-2 and cigarette smoke increases infection severity and alters the stem cell-derived airway repair response. *Cell Stem Cell* **27**, 869–875.e4 (2020).

66. G. I. Lee, J. Saravia, D. You, B. Shrestha, S. Jaligama, V. Y. Hebert, T. R. Dugas, S. A. Cormier, Exposure to combustion generated environmentally persistent free radicals enhances severity of influenza virus infection. *Part. Fibre Toxicol.* **11**, 57 (2014).

67. S. Jaligama, J. Saravia, D. You, N. Yadav, G. I. Lee, B. Shrestha, S. A. Cormier, Regulatory T cells and IL10 suppress pulmonary host defense during early-life exposure to radical containing combustion derived ultrafine particulate matter. *Respir. Res.* **18**, 15 (2017).

68. U. Karakus, M. Crameri, C. Lanz, E. Yángüez, Propagation and titration of influenza viruses. *Methods Mol. Biol.* **1836**, 59–88 (2018).

69. H. Ye, Z. Shen, M. Wei, Y. Li, Red blood cell hitchhiking enhances the accumulation of nano- and micro-particles in the constriction of a stenosed microvessel. *Soft Matter* **17**, 40–56 (2021).

70. X. Duan, J. Lu, K. Zhou, J. Wang, J. Wu, G. Fu Gao, M. Fang, NK-cells are involved in thymic atrophy induced by influenza A virus infection. *J. Gen. Virol.* **96**, 3223–3235 (2015).

71. G. Li, K. K. H. Y. Ho, Y. Y. Zuo, Relative dye adsorption method for determining the hydrophobicity of nanoparticles. *J. Phys. Chem. C* **126**, 832–837 (2022).

72. J. Gao, M. Sanchez-Purra, H. Huang, S. Wang, Y. Chen, X. Yu, Q. Luo, K. Hamad-Schifferli, S. Liu, Synthesis of different-sized gold nanostars for Raman bioimaging and photothermal therapy in cancer nanotheranostics. *Sci. China Chem.* **60**, 1219–1229 (2017).

73. S. Wang, J. Li, M. Chen, L. Ren, W. Feng, L. Xu, X. Chen, T. Xia, N. Zheng, S. Liu, Palladium nanoplates scotch breast cancer lung metastasis by constraining epithelial-mesenchymal transition. *Natl. Sci. Rev.* **8**, nwaa226 (2021).